Nano Research

Open Access

Research Article

Tunable microwave absorption in layered antiferromagnetic topological insulator $MnBi_2Te_4$ via progressive defect engineering

Guoliang Huang[1], Dawei Li[1], Panpan Zhang[1,3] ✉, Yunbing Sun[2,4], Jiahao He[1], Zhengsen Jing[1], Yulong Shen[1], Jumeng Wei[5], Yang Wu[1] ✉, and Ningning Song[1] ✉

[1] *College of Mathematics and Physics, Beijing University of Chemical Technology, Beijing 100029, China*
[2] *School of Physical Science and Technology, Baotou Teachers' College, Baotou 014030, China*
[3] *Beijing TongMei XTAL Technology CO., LTD., Beijing 101100, China*
[4] *Key Laboratory of Magnetism and Magnetic Materials at Universities of Inner Mongolia Autonomous Region, Baotou Teachers' College, Baotou 014030, China*
[5] *College of Chemistry and Materials Engineering, Anhui Science and Technology University, Bengbu 233030, China*

Cite this article: *Nano Research*, **2026**, *19*, 94908362. https://doi.org/10.26599/NR.2026.94908362

ABSTRACT: As an intrinsic magnetic topological insulator, $MnBi_2Te_4$ (MBT) has garnered significant attention owing to its unique magnetic and topological properties. However, the mechanism by which oxygen-doping modulates the transport properties in MBT remains unclear. The electromagnetic wave (EMW) absorption performance of MBT and the related attenuation mechanism lack clarification. Here, a progressive oxygen regulation strategy is proposed for MBT for the first time, achieving broad high-frequency EMW attenuation at small thickness. The EMW attenuation performance is synergistically manipulated by multiple factors, such as morphology, defect and conductivity, which significantly enhances its polarization loss and optimizes impedance matching. It is demonstrated that the extent of oxidation doping (i.e., the number of oxidized layers and types of oxidized bonds) significantly influences its intrinsic conductivity and polarization loss. Accordingly, the surface oxidized MBT exhibited an effective absorption bandwidth of 3.63 GHz (1.31 mm thickness), representing a 61% enhancement compared to the pristine MBT. Furthermore, the radar cross section is reduced by −25 dB across an ultra-wide angular range of −90°–90°. This work not only elucidates the distinct role of oxidative doping in modulating the intrinsic conductivity and EMW absorption, but also provides a feasible strategy for mitigating electromagnetic interference via MBT.

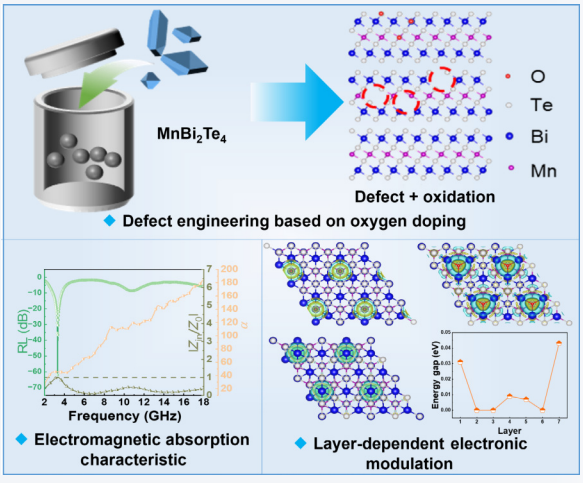

KEYWORDS: $MnBi_2Te_4$, antiferromagnetic topological insulator, microwave absorption, conductivity, defect engineering

1 Introduction

Artificial intelligence driven by integrated electronics and wireless electromagnetic communication have significantly enhanced the convenience and intelligence of daily life, particularly those currently operating in frequency bands (12–18 GHz) such as radar, satellite and cellular communication networks. Meantime, the issues of electromagnetic interference, conducted interference, signal distortion, and data transmission errors are closely interrelated and critically impact the performance and reliability of modern electronic and communication systems, which demands urgent resolution [1–3]. Electromagnetic wave (EMW) absorbing materials, which possess the capability to absorb EMW, play a critical role in mitigating electromagnetic radiation pollution [4]. Thus, to ensure device reliability and signal integrity, it is imperative to develop microwave-absorbing materials specifically tailored in this frequency band (12–18 GHz). Based on the absorption mechanism, EMW absorbing materials are primarily categorized as magnetic loss and dielectric loss absorbers. For magnetic loss absorbers, methods such as morphology control [5], composition tailoring [6], and synthesis techniques [7] have been used to

Received: October 15, 2025; **Revised:** November 30, 2025
Accepted: December 19, 2025

✉Address correspondence to Panpan Zhang, luckyfoe@yeah.net; Yang Wu, wuy@buct.edu.cn; Ningning Song, songnn@buct.edu.cn

enhance magnetic properties by manipulating shape or magnetocrystalline anisotropy. Whereas the Snoek's limit fundamentally constrains further improvements in their microwave attenuation ability. Dielectric loss absorbers exhibit excellent microwave attenuation ability owing to their high conductivity and dielectric performance. At the same time, high conductivity often leads to significant impedance mismatch between free space and the absorber, causing most EMW to reflect off its surface. Moreover, as the primary determinants of EMW absorption performance, the simultaneous realization of strong attenuation capacity and superior impedance matching remains fundamentally challenging for both magnetic and dielectric absorbers. Currently, a prevailing strategy to address these challenges is to form composite absorbers by integrating magnetic and dielectric components. The most extensively studied EMW absorbers at present are composites that combine magnetic nanomaterials (e.g., ferrite [4], magnetic alloys [8]) with various dielectric components, such as carbonaceous materials [9], MXene [10], high entropy alloy [11, 12], transition metal dichalcogenide [13, 14], and dielectric ceramic materials [15, 16]. However, the magnetic loss capacity was inevitably weakened or diluted after introduction of dielectric ingredients. Furthermore, the complex synthesis processes, substantial expense and extremely low yield of these materials hinder their further applications. Thus, there is still a long way to obtain satisfactory EMW absorber by traditional magnetic/dielectric materials, and it's crucial to seek a new idea to develop new materials with favorable EMW absorption performance.

In recent years, topological insulators (TIs) have attracted significant attention due to their metallic surface states, insulator bulk properties and exotic physical characteristics [17]. These materials exhibit surface states with energy levels above conduction band edge, leading to the formation of electron accumulation layers near surface [18, 19]. The inherent high dielectric constants of TIs can be complemented by substantial dielectric loss though adjusting the conductive surface states within their nanostructures. Thus, many TIs are implicit of excellent microwave absorption properties [17, 20–22]. In 2013, intrinsic antiferromagnetic TI $MnBi_2Te_4$ (MBT) were synthesized, which exhibits a septuple-layered structure with a Te-Bi-Te-Mn-Te-Bi-Te stacking sequence [23]. Since then, as a member of van der Waals (vdW) layered materials, MBT has become a star material due to the interplay between intrinsic magnetism and nontrivial topology that results in an emerging quantum phenomenon, enabling potential applications in dissipationless electronic and quantum computing [24, 25]. Despite these advances, there are several outstanding questions regarding the practical application of MBT. (i) The MBT surface is highly sensitive to air exposure and even to trace oxygen/water levels in a controlled environment such as a glovebox [26]. Extremely stringent conditions are therefore required to protect the surface state of MBT materials. (ii) The magnetic properties display a pronounced odd-even layer-number dependence, originating from its A-type antiferromagnetic structure [27]. Odd-layer MBT samples can host the quantum anomalous Hall state, while even-layer samples may exhibit an axion insulating behavior [28, 29]. Achieving uniform and large area synthesis of MBT materials with precise layer control has proven difficult. (iii) Certain topologies states (such as the quantum anomalous Hall effect) and magnetic performance can only be observed under very extreme experimental conditions, e.g., at very low temperatures or very strong external magnetic field [24, 30]. Thus, developing new electric/magnetic functionalities in MBT materials under ambient conditions is therefore critically important for practical applications.

MBT exhibits a wider range of intriguing electromagnetic properties compared to other TIs. Its electronic topological characteristics arise from the Bi–Te bilayers, whereas long-range magnetic ordering originates from the Mn^{2+} ion sublattice. Owing to these features, MBT is predicted to demonstrate excellent microwave absorption performance. However, current studies on its behavior in high-frequency electromagnetic fields are still limited, particularly concerning the underlying microwave absorption mechanisms. Li et al. [31] fabricated MBT/carbon fiber composite via a components integration approach, which achieved a maximum effective absorption bandwidth (EAB) of 2.6 GHz at 0.9 mm and a minimum reflection loss (RL_{min}) of −38.4 dB at 1.2 mm. In addition to components integration, structural modification technique, such as morphology control, elemental doping and defect engineering, serve as another important strategy to effectively boost microwave absorption performance [32, 33]. Specifically, defect engineering strategically introduces crystallographic imperfections, including point defects (e.g., oxygen vacancies), substitutional (via ion doping) and isolated atomic defects. These defects establish effective polarization mechanisms (interfacial polarization and dipole polarization), which optimize dielectric loss characteristics of absorbers, thereby enhancing their EMW attenuation performance [34]. Du et al. fabricated Co@MSC nanoparticles with abound heterogeneous interfaces and defect by precisely controlling oxidation duration, which endowed the material with exceptional conductive loss and defect-induced polarization [35]. Wang et al. designed carbon nanotubes and graphene with controllable defects via pyrolytic reduction to balance conduction loss and polarization loss, thereby enhancing their microwave absorption performance [36]. Shu et al. activated basal inert sites in iron telluride (FeTe) flakes through oxygen plasma-mediated dual-defect engineering. This treatment created abundant polarization centers, triggering charge redistribution and increased dipole density, and realizing an optimal absorption performance of −69.9 dB at a thickness of 2.2 mm [37]. Pan et al. created structural defects and carbon-oxygen dipoles in carbon nanocoils (CNCs) by a thermal oxidation strategy to induce local charge redistribution and active polarization behavior. Benefiting from the synergistic effects of structural defects and oxygen dopants, a broad EAB of 7.3 GHz at a low filling ratio of merely 3 wt.% was achieved [38]. Furthermore, the moderately oxidized layered MBT nanosheets exhibits excellent electrochemical performance with a high reversibility capacity (393.1 $mAh \cdot g^{-1}$), outstanding rate performance and cycle stability [39]. Nevertheless, the impact of surface oxide doping on their microwave absorption performance remains unexplored. A comprehensive investigation is required to uncover the corresponding dielectric/magnetic loss mechanisms and practical microwave applications based on MBT.

Compared to conventional defect-engineering methods, high-energy ball milling represents an eco-friendly and progressive approach for controlled constructing defect engineering. The duration of high-energy ball milling directly enables effective gradient defect modulation [40]. In this work, we successfully prepared progressively oxidized MBT micro-flakes via high-energy ball milling method. The defect engineering, dominated by oxidation doping, for precisely tuning microwave absorption performance of MBT are investigated. (1) We conducted a systematic investigation into the regulatory mechanism of oxidation

doping on the intrinsic conductivity of MBT. (2) The extent of oxidation doping (i.e., the number of oxidized layers and types of oxidized bonds) were significant for intrinsic conductivity and polarization loss. (3) The defect engineering significantly enhanced defect-induced polarization and interfacial polarization in MBT, thereby optimizing its impedance matching characteristics. Specifically, the 50 h ball-milled MBT obtained satisfactory microwave absorption ability achieving a RL_{min} of −61.99 dB at 3.30 GHz and EAB_{max} of 3.63 GHz, which increase by 61% compared to 2.25 GHz bandwidth for the original MBT. In addition, the RCS was reduced by −25 dB across an ultra-wide angular range of −90°–90°. These results yield critical insights that expand the scope of topological insulator research and their practical deployment in microwave absorption technologies, simultaneously underscoring the efficacy of defect engineering in designing next-generation microwave-absorbing materials.

2 Experimental section

2.1 Synthesis of MBT single crystal

The methods of growing bulk van der Waals single crystal materials include solid-phase melting approach [41], chemical vapor transport method (CVT) [42] and flux method [43]. In this work, the blocky MBT crystal was synthesized via a solid-phase melting approach using highly purified manganese (Mn), bismuth (Bi), and tellurium (Te) powders. At first, high-quality Bi_2Te_3 and MnTe were synthesized via a solid-state melt-growth approach. High-purity elemental precursors (Bi/Te for Bi_2Te_3 and Mn/Te for MnTe) were accurately weighed in their respective stoichiometric ratios, homogenized thoroughly inside an argon-filled glovebox, and then transferred into quartz ampoules. To prevent contamination from oxygen, water vapor, and other atmospheric impurities, the ampoules were evacuated and flame-sealed. For Bi_2Te_3, the sealed ampoule was first heated to 400 °C for 24 h, then ramped to 800 °C for another 24 h, followed by cooling to room temperature. For MnTe, the ampoule was heated to 830 °C for 9 h, then ramped to 870 °C and maintained at this temperature for 48 h, after which it was removed from the furnace and quenched in ambient air.

The $MnBi_2Te_4$ crystal was synthesized primarily by the direct reaction of pre-synthesized Bi_2Te_3 and MnTe precursors via a high-temperature solid-state melt route. Specifically, Bi_2Te_3 and MnTe powders were mixed in a stoichiometric 1:1 molar ratio, transferred into quartz ampoules, subsequently evacuated to remove residual gases, and flame-sealed to ensure a contamination-free environment. The sealed ampoules were heated to 900 °C at a ramp rate of 100 °C·h^{-1}, resulting in a fluid Bi–Te melt that acts as a self-flux to significantly promote atomic mobility within the reaction system. Mn, initially present as MnTe, is thermodynamically favored to partially dissolve into the Bi–Te melt or migrate via solid-state diffusion at particle interfaces; upon dissolution, Mn is rapidly homogenized throughout the ampoule by the molten phase. When the local chemical potential enters the stability range of $MnBi_2Te_4$, well-defined $MnBi_2Te_4$ nuclei are formed at the melt or solid–liquid interfaces. The furnace temperature was then rapidly cooled to approximately 590 °C and maintained at this temperature for 7 days. During the isothermal hold, the melt gradually become supersaturated with Mn, Bi, and Te, leading to the nucleation of $MnBi_2Te_4$. This nucleation process generated in-plane ordered layered structure, which subsequently grew layer-by-layer along *c*-direction to form bulk $MnBi_2Te_4$ crystals. After the isothermal dwell, the samples were removed from the furnace and quenched in ambient air, yielding high-quality $MnBi_2Te_4$ single crystals.

2.2 High energy ball milling treatment

High-energy planetary ball mill (FOCUCY, F-P400) was used for high-energy ball milling. Then, MBT single crystal and agate balls were loaded into an agate ball milling tank at a 2.5:1 ball-to-material mass ratio, with proper amount of anhydrous ethanol as control agent. To prevent overheating, a cycle ball milling (1 h operation/15 min pause) was implemented, with rotation speed maintained at 900 revolutions per minute. After 42 h ball milling, the sample was washed three times by centrifugation with anhydrous ethanol, and then dried at 50 °C for 12 h. The prepared MBT sample was marked as M42h. Similarly, samples M50h and M58h were prepared following the same protocol, with the sole variation of ball milling time: 50 and 58 h, respectively. The MBT single crystal without ball milling was designated as M0h.

2.3 Characterizations

Scanning electron microscopy (SEM, SU5000) was applied to analyze the micro-nano morphology of as-prepared samples with an accelerating voltage of 10 kV. Transmission electron microscopy (TEM) and high-resolution transmission electron microscopy (HRTEM) were performed to analyze the fine nanostructure and crystallite of materials with a JEM 2100F electron microscope (accelerating voltage of 200 kV). The crystal structure of all samples was characterized by X-ray diffraction (XRD, Bruker D2, Cu-Kα radiation; λ = 1.54059 Å, 30 kV/10 mA). The Raman spectra were measured by a LabRAM HR Evolution Raman spectrometer (Horiba, Japan) with a laser excitation of 532 nm, covering wave range of 40–2500 cm^{-1}. All XPS spectra were collected with a Kratos Axis Ultra^{DLD} spectrometer (Krato Analytica-A Shimadzu Group Company), using a monochromatic Al Kα X-ray source ($h\nu$ = 1486.6 eV). The full-spectrum scanning pass energy is 150 eV, and the step size is 1 eV. The narrow-band scanning pass energy is 50 eV, and the step size is 0.1 eV. All binding energies were referenced to the carbon 1s peak at 284.8 eV. EPR measurements were performed with a Bruker A 300 electron paramagnetic resonance spectrometer. The electrochemical impedance spectrum (EIS) was measured by CHI660E electrochemical workstation from 10^{-2} to 10^{5} Hz, which is in the potential disturbance of open circuit voltage in a typical three-electrode system. Na_2SO_4 aqueous solution (1 M) was used as electrolyte, platinum mesh (1.0 cm × 1.0 cm) was used as counter electrode, and Ag/AgCl electrode was used as reference electrode. The sample was evenly mixed with polyvinylidene fluoride according to the mass ratio of 5:1, and then pressed into a piece with a diameter of 13 mm as the working electrode. Open circuit potential (OCP) test lasts for 30 minutes to ensure the stability and accuracy of subsequent electrochemical impedance spectroscopy (EIS). The magnetization as a function of magnetic field was measured by a Physical Property Measurement System (PPMS-9T, Quantum Design, USA) and carried out at 300 K with magnetic fields between −1.0 and +1.0 T. The EM parameters at 2–18 GHz were measured by a vector network analyzer (VNA, E5071C, Agilent) at room temperature using a coaxial transmission-reflection method. To obtain the electromagnetic parameters of $MnBi_2Te_4$ single crystal [31], $MnBi_2Te_4$ single crystal were grounded with mortar to obtain $MnBi_2Te_4$ crystal powder. The corresponding toroidal-shaped samples with a 7.00 mm outer diameter and a 3.04 mm inner

diameter at a thickness of 2.00 mm were prepared by mixing the obtained samples with paraffin wax at a weight ratio of 4:1 (the total mass of the sample and paraffin is uniformly controlled at 150 mg). The electromagnetic parameters of samples at other thicknesses were calculated based on that of 2.00 mm. The resolution of the thickness was 0.01 mm.

3 Results and discussion

3.1 Morphology reconstruction and surface defect

MBT micro-flakes were prepared by controlled high energy ball milling of MBT crystal. The macroscopic morphology, microstructure and elemental distribution of MBT crystal are shown in Fig. S1 in the Electronic Supplementary Material (ESM). The MBT crystal exhibits a distinct metallic luster on its surface (Figs. S1(a) and S1(b) in the ESM) with a layered structure visible beneath (Figs. S1(c) and S1(d) in the ESM). Elemental mapping analysis (Fig. S1(e) in the ESM) reveals a homogeneous distribution of all elements in the as-prepared MBT crystal, with no signs of aggregation. Figure 1 shows the SEM images and elemental mapping results of MBT micro-flakes after different ball milling times. After 42 h of ball milling (Fig. 1(a)), M42h sample exhibits irregular sheet-like morphology, with a significant multilayer structure (Fig. 1(b)). During high-energy ball milling, MBT crystals undergo shearing, compression, impact and frictional forces, leading to shear deformation. Consequently, irregular sheet-like particles formed under the combined mechanical action of the agate can and grinding balls. Figure S1(c) in the ESM and Fig. 1(b) conform that as-prepared MBT crystal is a typical vdW layered material. The thickness distribution of sample M42h predominantly

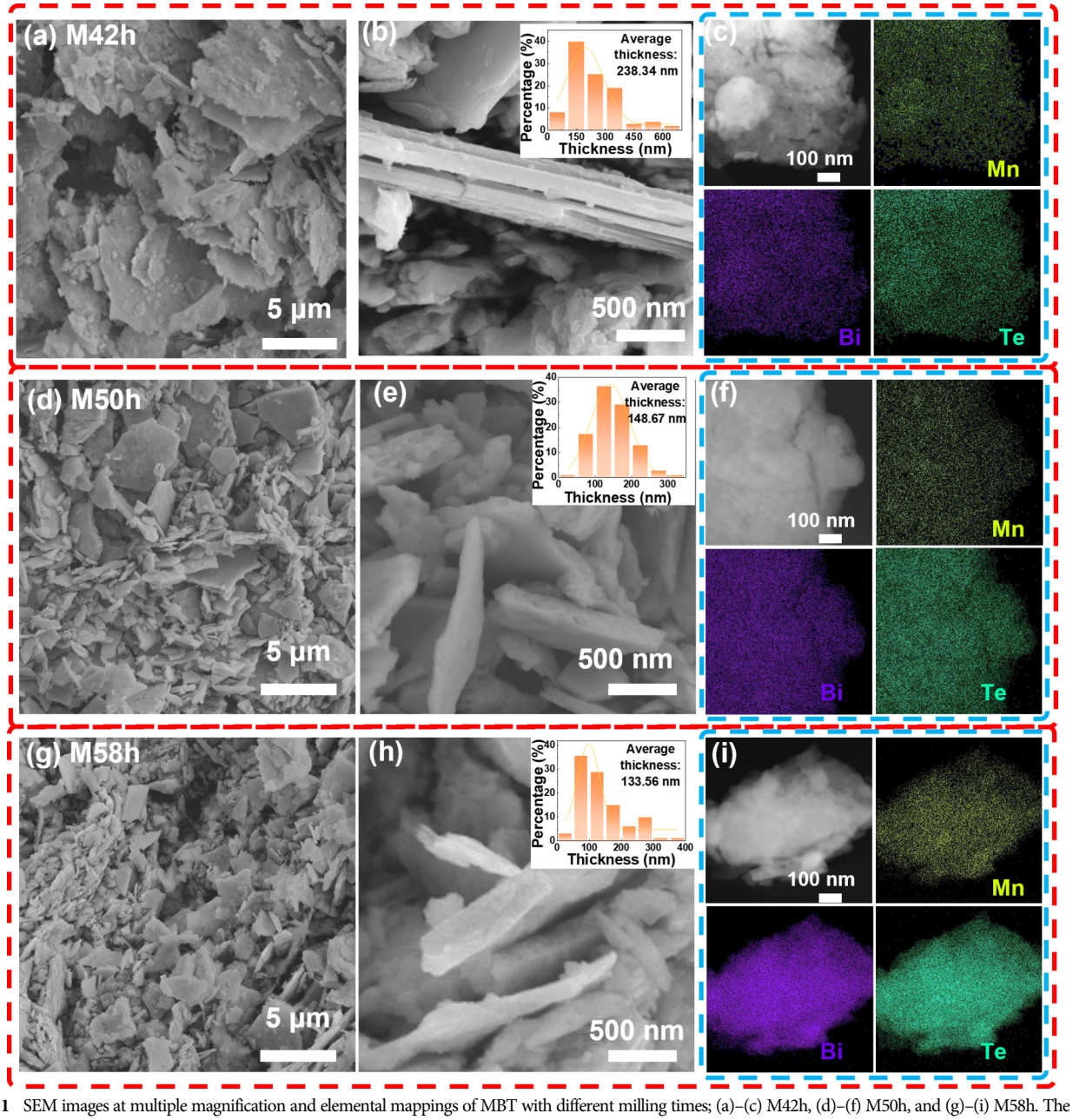

Figure 1 SEM images at multiple magnification and elemental mappings of MBT with different milling times; (a)–(c) M42h, (d)–(f) M50h, and (g)–(i) M58h. The insets are the thickness distributions of M42h, M50h, and M58h, respectively.

ranges from 150 to 250 nm, with an average value of 238.3 nm (inset of Fig. 1(b)). As the ball milling time extends to 50 h, the average thickness of sample M50h decreases to 148.7 nm, concentrated between 125 and 175 nm (inset of Fig. 1(e)). The dimension of M50h sample tends to decrease too. This is because when the thickness of the micro-sheets decreases below a critical threshold, fragmentation becomes the dominant mechanism [44]. Consequently, prolonged ball milling fractures the cold-welded sheets, reducing the dimension of the MBT micro-sheets. Especially after 58 h of ball milling, the dimension of the micro-sheets further decreased, generating abundant smaller irregular fragments. The average thickness declined to 133.6 nm, with primary concentration in the 75–125 nm range (inset of Fig. 1(h)). A significant enhancement in specific surface area was achieved in the scaled-down MBT micro-flakes due to the precise control over their thickness and dimensions. The increased surface area not only enhances interface dipole interactions but also modulates charge transport behavior due to the unique surface/bulk conductive state in MBT. Notably, the thickness of all MBT micro-flakes is substantially smaller than skin depth, which helps suppress eddy current effects on their EMW absorption performance [45]. The corresponding EDS mappings for Mn, Bi, Te and O of samples M42h, M50h and M58h in Figs. 1(c), 1(f), and 1(i), and Fig. S2 in the ESM reveal uniform distributions of all four elements, and no elemental aggregation can be observed after ball milling.

Beyond morphology and size control, ball milling simultaneously introduces defects on MBT surfaces, as schematically illustrated in Fig. 2(a). TEM and HRTEM analyses were performed to investigate the microstructure of MBT micro-flakes. The TEM image of sample M0h in Fig. S3(a) in the ESM reveals that as-prepared MBT sample without ball milling treatment exhibits a distinct layered structure. Ordered lattice fringes can be clearly observed in the HRTEM image in Fig. S3(b) in the ESM, demonstrating the high degree of crystallinity for M0h sample. The lattice fringe spacing is 0.229 nm (Figs. S3(d) and S3(e) in the ESM), corresponding to the (1 0 14) crystal plane of MBT. Figure 3(b) and Figs. S4 and S5 in the ESM reveal co-existing of amorphous domains (lacking lattice fringes) and crystalline regions (with distinct 0.28 nm lattice spacing) in all ball-milled samples M42h-M58h. In the crystalline regions (Figs. 2(d1) and 2(d2), and Figs. S4(c1), S4(c2), S5(c1), and S5(c2) in the ESM), the accurately measured lattice fringe spacing

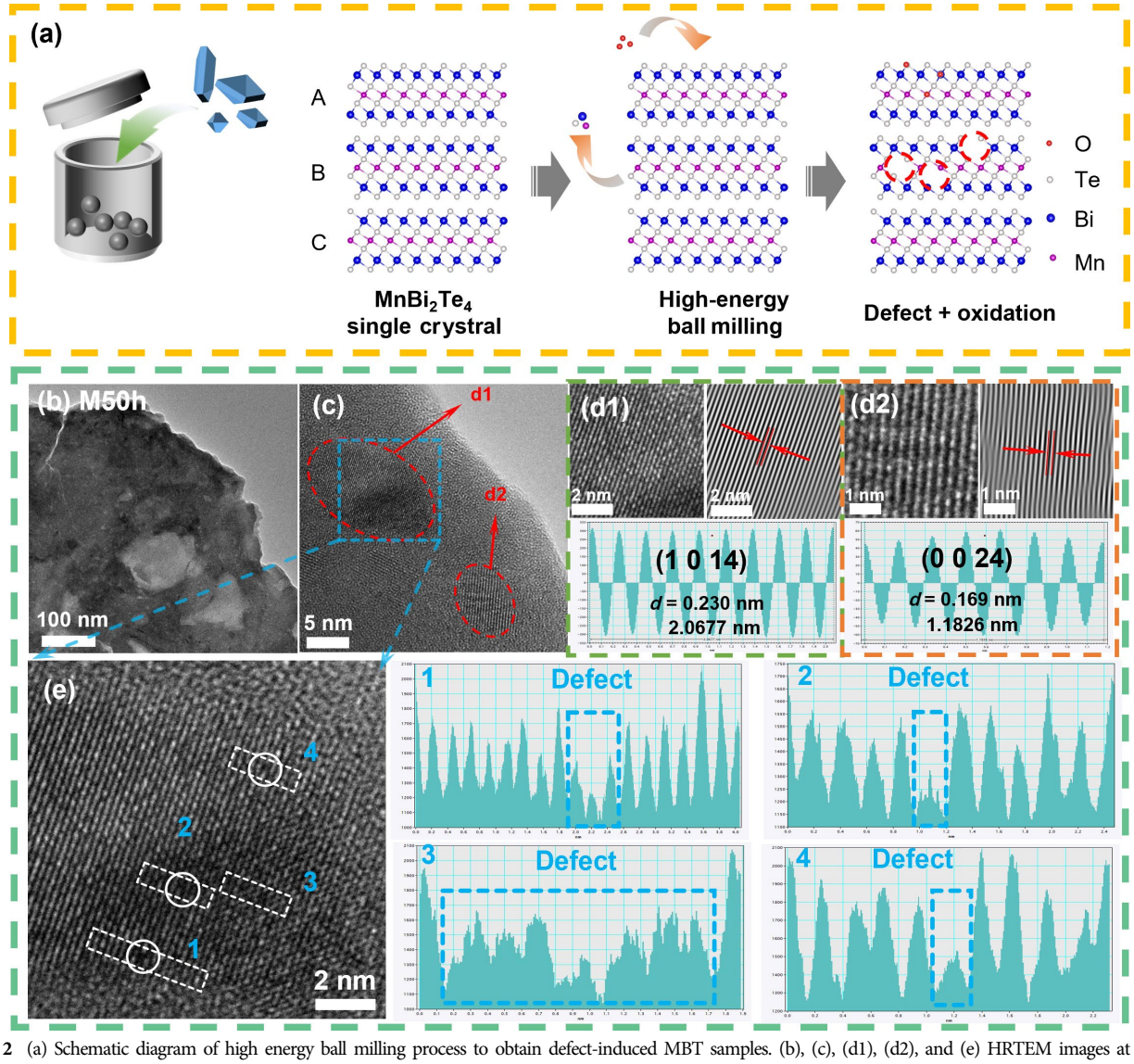

Figure 2 (a) Schematic diagram of high energy ball milling process to obtain defect-induced MBT samples. (b), (c), (d1), (d2), and (e) HRTEM images at various magnifications, along with corresponding intensity profiles derived from inverse fast Fourier transform analyses of the selected regions.

d = 0.341, 0.329, 0.230, and 0.169 nm, which can be assigned to the (0 0 12), (1 0 7), (1 0 14), and (0 0 24) crystallographic planes of MBT, respectively. Moreover, prolonged ball milling leads to progressive expansion of amorphous regions. These crystalline-amorphous heterostructures possess contrasting dielectric properties, enabling the construction of abundant heterogeneous interfaces [46]. These heterogeneous interfaces, in turn, facilitate space charge accumulation and non-uniform distribution. Space charges at these interfaces undergo repeated charge polarization under high-frequency EMW, similar to a parallel-plate capacitor, effectively dissipating electromagnetic energy [47]. Simultaneously, numerous lattice defects and lattice distortions exist in the crystalline regions. To elucidate these defects, Fig. 2(e) presents an enlarged view of the crystalline region for sample M50h (notably marked in blue in Fig. 2(c)). Fourier transform analysis reveals marked attenuations in peak intensity: three attenuated peaks in region 1, one attenuated peak in regions 2 and 4, and multiple attenuated peaks in region 3, representing three atomic defect in region 1, single atomic defect in regions 2 and 4, and clustered atomic defect in region 3, respectively. Defect distributions in M42h and M58h samples were shown in Figs. S4(d) and S5(d) in the ESM. These defect distributions reveal that prolonged ball milling time introduces a greater density of defects, which are predominantly oxygen impurities resulting from milling-induced surface oxidation, along with mechanically induced crystal defects (such as dislocations, stacking faults). Under high-frequency electromagnetic fields, these defects can capture charge carriers and disrupt the equilibrium of carrier charge distribution, thereby inducing polarization processes and dissipating EMW energy. This energy dissipation mechanism is classified as defect-induced polarization [48]. High-density crystalline-amorphous heterointerfaces, lattice defects and oxygen vacancies in MBT micro-layers synergistically enhance interfacial polarization, dipolar polarization and defect-induced polarization. These polarization relaxations can effectively coordinate and balance the real and imaginary parts of the complex permittivity, thereby improving impedance matching, and allowing more EMW to be dissipated rather than reflected back into free space.

MBT can be regarded as Bi_2Te_3 quintuple layer intercalated with MnTe bilayer, consisting of septuple layer stacking via vdW forces (Fig. 3(a)). XRD was carried out to determine the phase and crystalline structure of as-grown MBT samples. The XRD pattern of finely ground MBT powder (M0h) in Fig. 3(b) matches the calculated XRD pattern of MBT ($R3m$ space group) with no detectable impurity peaks, confirming the high purity of as-prepared MBT crystal. Its lattice constants a = 4.36 Å and c = 40.92 Å [23, 49]. The positions of main diffraction peaks and the corresponding crystal planes are listed in Table S1 in the ESM. After prolonged high-energy ball milling, the XRD patterns of M42h, M50h and M58h samples retain diffraction peaks exclusively

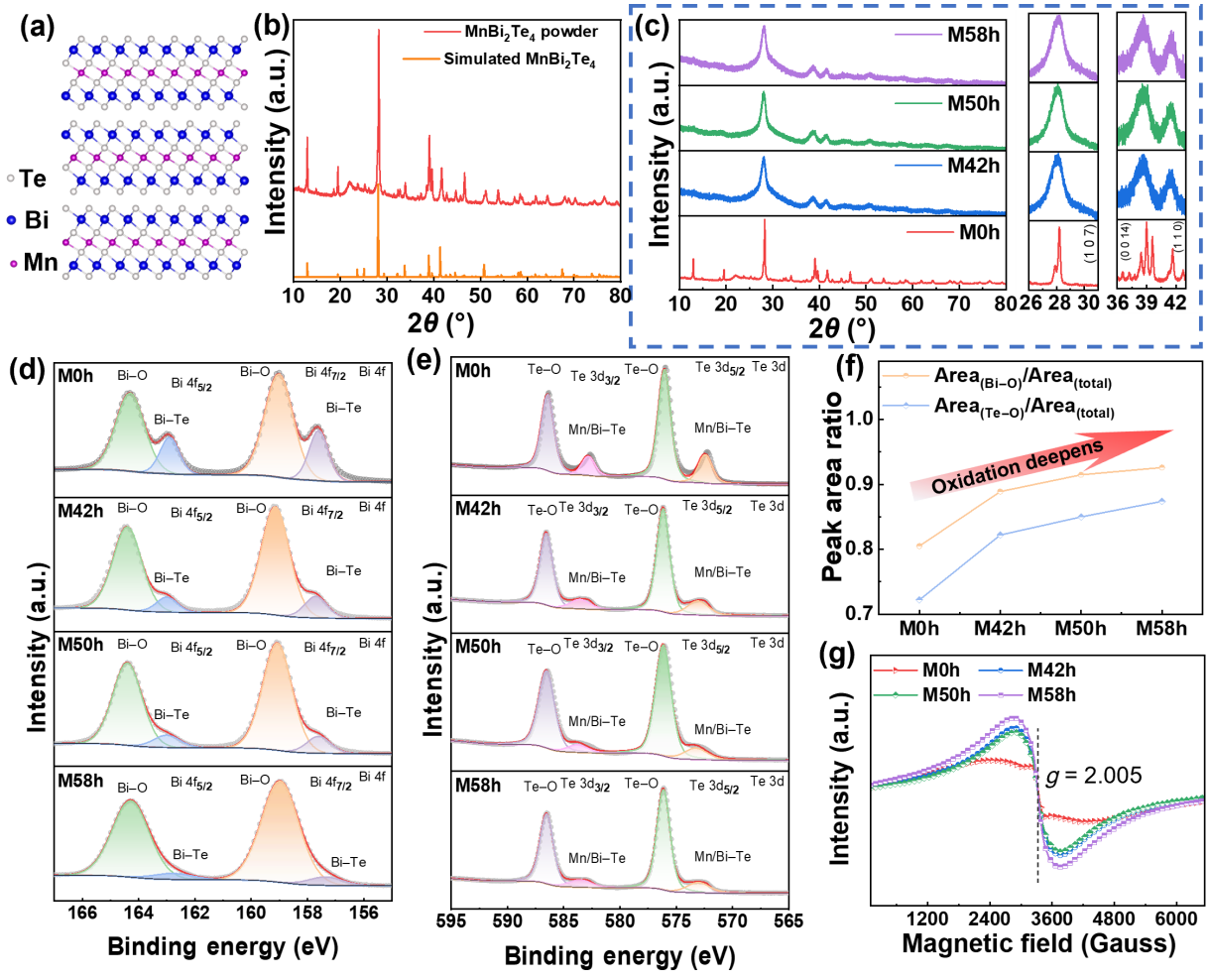

Figure 3 (a) Atomic structure of MBT. (b) and (c) XRD patterns, high-resolution XPS spectra of (d) Bi 4f and (e) Te 3d, and (g) EPR spectra for M0h, M42h, M50h, and M58h; (f) relative area ratios of Te–O and Bi–O peak area to total Te 3d and Bi 4f peak intensities.

corresponding to the (1 0 7), (0 0 14), and (1 1 0) crystal planes, with all secondary peaks completely vanished. Besides, the diffraction peaks of M42h, M50h and M58h gradually broaden with increasing grinding time. This phenomenon originates from oxygen vacancies caused by surface oxidization, along with lattice defects (e.g., dislocations, vacancies) and amorphous nanodomains generated due to accumulated internal strain in MBT during high-energy ball milling [50]. The reduced particle size of MBT micro-layers also contributes to the observed broadening of XRD diffraction peaks, as quantified by the Debye–Scherrer formula. Figure S6(a) in the ESM displays the Raman spectra of ball-milled MBT samples (M42h-M58h), exclusively exhibiting A_{1g} vibrational modes at 138 cm^{-1} (A^3_{1g}) and 116 cm^{-1} (A^2_{1g}). The absence of other modes suggests the reduced effective oscillator density per unit area which might be caused by the defect-mediated suppression of Raman-active vibrations [27, 30, 51].

X-ray photoelectron spectroscopy (XPS) was employed to characterize the elemental composition and chemical surface states of the samples. In Fig. S6(b) in the ESM, characteristic peaks corresponding to Mn, Te and Bi elements were detected at 642–653, 576–587, and 158–165 eV, respectively, indicating the presence of these elements in all samples. The XPS spectrum of Mn 2p in Fig. S5(c) in the ESM displays Mn $2p_{3/2}$ and Mn $2p_{1/2}$ components. Mn $2p_{3/2}$ and Mn $2p_{1/2}$ peaks were each deconvoluted into four subpeaks, labeled M1–M4 and M1'–M4', respectively. M1 and M1' peaks located at 640.1 and 651.8 eV are attributed to oxidation products generated upon dissociation of Mn–Te bonds [39]. M2 and M2' peaks located at 641.1 and 653.4 eV are assigned to Mn^{2+} species within the Mn–Te bonds. The satellite peaks M3/M3' at 642.5 eV/655.5 eV and M4/M4' at 645.8 eV/658.6 eV originate from charge transfer between the outer shells of Te and the unfilled 3d shells of Mn during the photoelectron process [41]. In the high-resolution Bi 4f XPS spectrum (Fig. 3(d)), the peaks at 159.0 and 164.3 eV correspond to Bi–O $4f_{7/2}$ and Bi–O $4f_{5/2}$ originating from oxidized MBT, respectively. While the peaks at 157.6 and 162.9 eV correspond to Bi $4f_{7/2}$ and Bi $4f_{5/2}$ of Bi^{3+} within Bi–Te bonds [52]. In Fig. 3(e), the Te 3d spectrum exhibits two main peaks at 572.3 eV (Te $3d_{5/2}$) and 582.7 eV (Te $3d_{3/2}$), corresponding to Te^{2+} in Bi–Te bonds and Mn–Te bonds, respectively. Two minor peaks at 575.9 eV (Te $3d_{5/2}$) and 586.3 eV (Te $3d_{3/2}$) are attributed to Te^{4+} in Te–O bonds, indicating the oxidation state of Te increasing from +2 to +4 upon exposure to air. This mild surface oxidation in MBT samples is consistent with the work reported before [53]. Figure 3(f) and Table S4 in the ESM quantitatively present the evolution of surface oxidation ratios (Bi–O/Bi–Te peak intensity ratios and Te–O/(Te–Mn + Te-Bi) peak intensity ratios) with ball milling times. Prolonged ball milling progressively reduces the fitted peak intensities of metallic bonds (Bi–Te, Mn–Te), while enhances those of oxide components (Bi–O, Mn–O, and Te–O). The oxygen vacancy concentration in MBT samples is further measured by electron paramagnetic resonance (EPR) spectroscopy, as shown in Fig. 3(g). The prominent peak intensity at g = 2.005 arises from free electrons trapped by oxygen vacancies [54–57]. Usually, the higher the peak intensity, the higher the level of defects in the crystal. It can be found that extended ball milling significantly increases concentration of oxygen vacancies in the MBT samples, evidenced by enhanced EPR signals in Fig. 3(g). The M58 sample exhibits the strongest EPR peak intensity, indicating the highest oxygen vacancy concentration among all samples. These results demonstrate that the oxidation degree of MBT can be effectively modulated by adjusting the ball milling duration. This is because that ball milling process fragments MBT crystals into micro-flakes, significantly increasing their specific surface area and air-exposed area (as evidenced by SEM images in Fig. 1), which accelerates surface oxidation through enhanced atmospheric oxygen interaction. The defects induced by abundant oxygen vacancies and polar chemical bonds disrupt the symmetry of electron–hole pairs, acting as dipole centers to generate dipole polarization, which significantly enhances dielectric loss properties and thereby improves microwave absorption capability to a certain extent [58].

3.2 The effect and mechanism of defect engineering on the microwave absorption performance of MBT

The EMW absorption properties of MBT powder (M0h) and ball-milled samples (M42h, M50h, and M58h) were evaluated using transmission line theory (Eqs. (S1) and (S2) in the ESM), as shown in Fig. 4 and Fig. S7 in the ESM. An optimal absorber should attenuate over 90% of incident EMW with RL below −10 dB, and the corresponding frequency range is considered the EAB. The non-ball-milled M0h sample (Figs. 4(a) and 4(d) achieves a RL_{min} of −61.41 dB at 4.40 GHz with a thickness of 3.42 mm, and a maximum effective absorption bandwidth (EAB_{max}) of 2.26 GHz (at 2.73 mm thickness). Ball milling induces significant changes on microwave absorption performance. Figures S7(a) and S7(c) in the ESM reveal that the M42h sample exhibits a RL_{min} of −28.34 dB (1.05 mm thickness/17.40 GHz), while its EAB_{max} reaches 4.02 GHz at 1.55 mm thickness. With increasing ball milling time to 50 h, the RL_{min} enhances to −61.99 dB (5.49 mm thickness/3.30 GHz), with EAB_{max} of 3.63 GHz at a thickness of 1.31 mm. Further prolonged milling beyond 50 h leads to noticeable performance degradation. The M58h sample (Figs. S7(b) and S7(d) in the ESM) demonstrates reduced absorption capability, achieving only RL_{min} = −19.26 dB at 3.00 GHz (6.00 mm thickness), with EAB_{max} = 2.28 GHz at 3.45 mm. A detailed comparison of RL_{min} and EAB_{max} across all samples in Fig. 4(c) reveals that M50h sample exhibits optimal reflection loss capability (RL_{min} = −61.99 dB), while the M42h sample achieves the best effective absorption bandwidth (EAB_{max} = 4.02 GHz). Compared to M0h sample, ball-milled process not only maintains strong reflection loss but also broadens the maximum effective bandwidth, enabling effective microwave attenuation over a wider range of frequencies. As a critical parameter for evaluating the practicality of microwave absorbers, a broad EAB_{max} enables the material to function across multiple frequency bands (e.g., radar and communication bands), enhancing adaptability to complex electromagnetic environments. Whereas EAB_{max} typically exhibits strong thickness dependence in most materials, which increases the need of customized material design. Figure 4(f) compares the EAB_{max} of M0h and M50h samples at different thicknesses. Contrary to conventional absorbers, both samples show limited thickness dependence in EAB_{max}. Notably, the M50h sample achieves broader EAB_{max} (~ Ku GHz) at reduced thicknesses (1.30–1.40 mm) compared to M0h.

Attenuation constant (α) and impedance matching ($Z = |Z_{in}/Z_0|$) represent two fundamental parameters governing microwave absorption performance in absorbers. Attenuation constant (α) quantifies an absorber's ability to convert EMW energy into other forms through dielectric and magnetic loss mechanisms (Eq. (S3) in the ESM). Figure 4(g) illustrates the α of MBT samples (M0h, M42h, M50h, and M58h) across the measure frequency range of

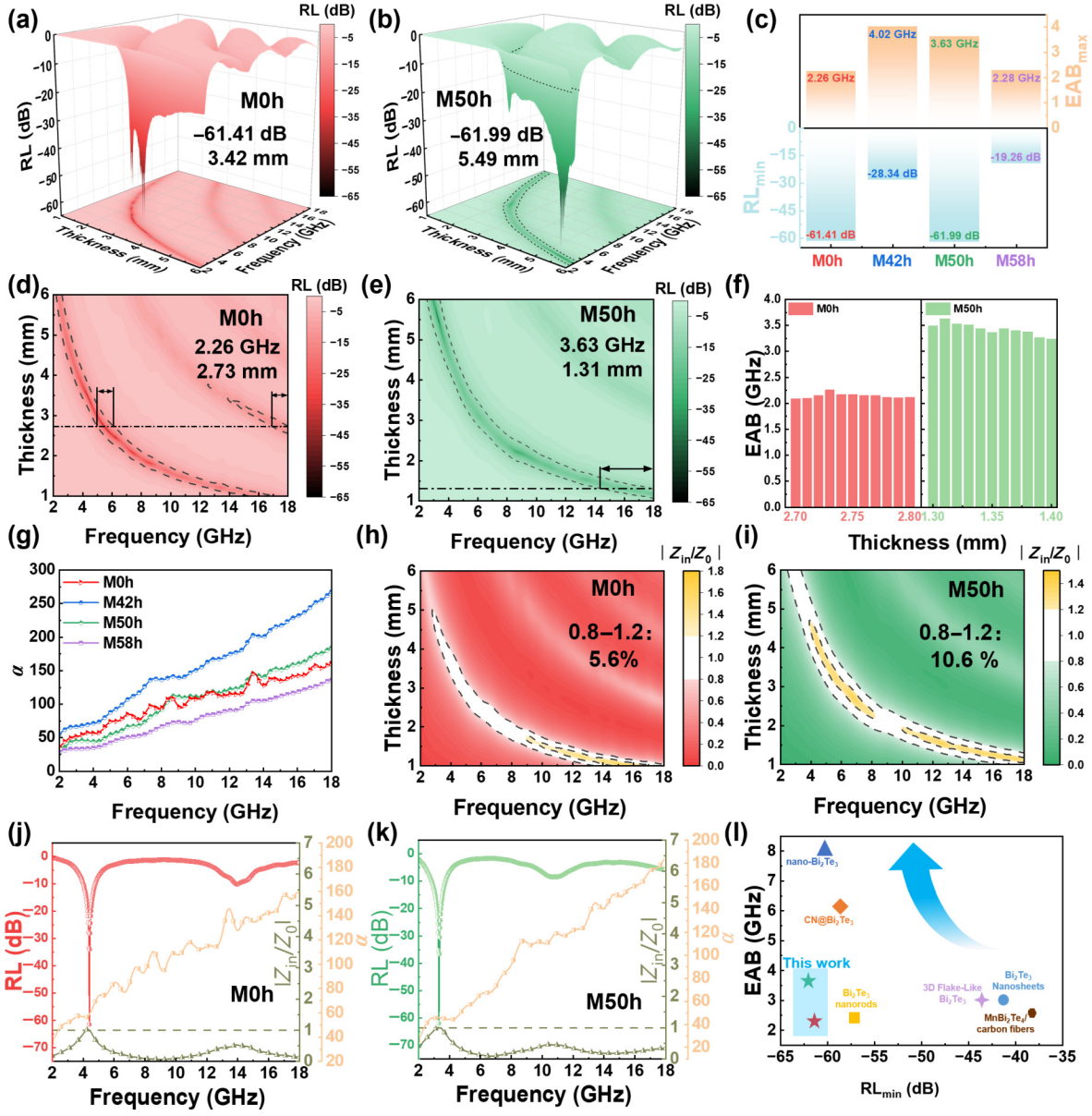

Figure 4 Frequency-dependent reflection loss 3D curves for sample (a) M0h and (b) M50h. Frequency dependent 2D contour distribution of reflection loss for sample (d) M0h and (e) M50h. (f) Thickness dependent EAB_{max} for samples M0h and M50h. (c) Comparison of RL_{min} and EAB_{max}. (g) Frequency dependent α values for all samples. Z contour plots for sample (h) M0h and (i) M50h. Comparison of RL curve, α and Z for samples (j) M0h and (k) M50h. (l) Microwave absorption performance of reported topological insulator absorbers on RL_{min} and EAB.

2–18 GHz. The α–f curves exhibit monotonic growth with rising frequency across all samples, indicating enhanced attenuation capability at higher-frequency. After 42 h of ball milling, sample M42h demonstrates a substantial increase in α compared to the unprocessed sample M0h. However, prolong ball milling beyond 42 h leads to a marked reduction of α values. Subsequently, M50h and M0h samples exhibit comparable attenuation performance. Further extension of milling time to 58 h (M58h) induces significantly diminished attenuation efficiency. Notably, although M42h sample exhibits superior EMW attenuation capability, its overall microwave absorption performance remains suboptimal. Extensive research indicates that excessively high α values frequently induce impedance mismatch, resulting in significant wave reflection at the air-absorber interface rather than effectively energy dissipation. Optimal impedance matching enables deeper EMW penetration into the absorber, serving as another critical requirement for efficient energy dissipation. To achieve superior absorption, the balance of attenuation capability and impedance matching characteristics need to be satisfied. The impedance matching (Z) characteristics can be described by Eq. (S4) in the ESM. The closer the Z value is to 1, the better the impedance matching of the EMW absorbing materials [59]. The practical optimum impedance matching condition is achieved when Z value falls within the range of 0.8 to 1.2 (defined as the effective absorption regime) [60]. Figures 4(h) and 4(i), and Figs. S7(e) and S7(f) in the ESM illustrate the normalized impedance Z values of as-prepared MBT samples across varying thicknesses and frequencies. The calculated effective absorption area ratios (white regions) for M0h, M42h, M50h, and M58h samples are 5.6%, 3.0%, 10.6%, and 5.1%, respectively. M50h sample displays superior matching

properties, whereas M42h sample exhibits the poorest impedance matching characteristics. Despite the strongest attenuation capability, the poorest impedance matching of M42h results in suboptimal microwave absorption performance. By contrast, M50h sample achieves optimal microwave absorption performance owing to its balanced impedance matching and robust EMW attenuation capability. M58h sample exhibits the weakest microwave absorption performance due to both inferior impedance matching and inadequate attenuation capability. To intuitively compare the relationship among microwave absorption performance, attenuation coefficient, and impedance matching, Figs. 4(j) and 4(k) present the frequency dependent RL, α and Z for samples M0h and M50h, respectively. The frequency corresponding to RL_{min} aligns well with the frequency where $Z \approx 1$. This further demonstrate that superior microwave absorption performance is closely correlated to absorber's impedance matching characteristics. Compared to previously reported topological insulator absorbers, the defect-engineered MBT samples processed by high-energy ball milling technique in this work exhibits superior reflection loss and broad effective absorption bandwidth (Fig. 4(l) and Table S5 in the ESM). Consequently, ball-milling induced defect engineering effectively modulates the attenuation capability of MBT samples, optimizes their impedance matching characteristics, and plays a critical role in enhancing their intrinsic microwave absorption performance.

Notably, dual-band absorption behavior is observed in MBT samples, characterized by two distinct minimum absorption peaks (RL_{min} peaks) coexisting at identical thicknesses, as evidenced in the frequency-dependent reflection loss (RL) curves with varying thicknesses in Fig. S8 in the ESM. The interference-based matching thickness was calculated using quarter-wavelength equation, as formulated in Eq. (S5) in the ESM. Figure S8 in the ESM illustrates that the experimental matching thickness via transmission line theory aligns well with the simulated interference-based thickness derived from the quarter-wavelength theory for all MBT samples. This agreement confirms that the samples satisfy the quarter-wavelength destructive interference model. Further analysis of these dual absorption peaks observed in the RL curves reveals that these dual absorption peaks originate from first-order interference absorption in the low-frequency region and second-order interference absorption in the high-frequency region. This indicates the existence of multi-level interference loss mechanisms in the MBT samples. In particular, M0h and M50h samples (Figs. S8(a) and S8(c) in the ESM) exhibit absorption characteristics dominated by strong first-order interference, with comparatively weaker second-order interference contributions. M42h sample exhibits moderate dual-band absorption under relatively balanced first- and second-order interference effects (Fig. S8(b) in the ESM), enabling effective absorption of EMW across two frequency bands. Upon extending ball-milling time to 58 h, M58h sample (Fig. S8(d) in the ESM) exhibits weak RL peaks induced by both first- and second-order interference. These results indicate that ball-milling induced defect engineering effectively modulates multi-level interference loss mechanisms, thereby optimizing microwave absorption performance.

To intrinsically elucidate the evolution of microwave absorption performance and loss mechanisms resulting from ball-milling-induced defect engineering in MBT samples, we investigated the electromagnetic parameters, relative complex permittivity ($\varepsilon_r = \varepsilon' - j\varepsilon''$) and complex permeability ($\mu_r = \mu' - j\mu''$). The real parts (ε' and μ') represent the capability of storing electrical and magnetic energy, whereas the imaginary components (ε'' and μ'') are related to the dissipation of electrical energy and magnetic energy. The microwave absorption mechanism is primarily governed by dielectric loss and magnetic loss. Magnetic loss can be quantified by the relative complex permeability and magnetic loss tangent ($\tan\delta_\mu = \mu''/\mu'$). The complex permeability components (μ' and μ'') of all four samples exhibit values close to 1 and 0, respectively, as demonstrated in Figs. S9(a) and S9(b) in the ESM. The magnetic loss tangent ($\tan\delta_\mu$) values in Fig. S9(c) in the ESM similarly fluctuate near zero. Additionally, all MBT samples exhibit negligible hysteresis at room temperature (Fig. S9(d) in the ESM), consistent with their antiferromagnetic nature. These results indicate that magnetic loss is negligible in the as-prepared MBT samples, and the primary loss mechanism is dielectric loss.

Dielectric loss can be quantified by the relative complex permittivity and dielectric loss tangent ($\tan\delta_\varepsilon = \varepsilon''/\varepsilon'$). As shown in Fig. 5(a), the real permittivity (ε') of all four samples decreases with increasing frequency, exhibiting a pronounced dispersion effects [61]. After 42 h of ball milling treatment, M42h maintains lower ε' values (24.70–15.27) compared to M0h (27.54–19.06) across 2–18 GHz range. Prolonged ball milling duration to 50–58 h further decreases the initial ε' value to 17.52 for M50h and 17.42 for M58h. Furthermore, the ε' values of M50h (17.52–13.14) and M58h (17.42–13.07) exhibit minimal variation from 2 to 18 GHz. This indicates that extending ball milling beyond 50 h produces negligible changes in ε' values of MBT samples. Figure 5(b) displays the frequency-dependent imaginary permittivity (ε'') of the four samples. All samples exhibit multiple peaks, indicating the presence of multiple polarization relaxation processes. The pristine sample M0h displays lower ε'' value (ranging from 7.54 to 0.41) compared to M42h sample (7.76–5.96). Further extending ball milling to 50 and 58 h results in a significant reduction of ε'' values (M50h: 2.60–4.40 and M58h: 2.76–3.05). According to the free electron theory, $\varepsilon'' = \sigma/(2\pi\varepsilon_0 f)$, the ε'' values of a material are positively correlated with its electrical conductivity, where ε_0 is the vacuum permittivity [62, 63]. Thus, the charge transfer resistance (R_{ct}) of MBT samples were quantitatively evaluated by electrochemical impedance spectroscopy (EIS) measurements [64–66]. The Nyquist plots (Fig. 5(d)) display AC impedance spectra of all samples. M58h exhibits the largest semicircle radius, indicating the slowest charge transfer kinetics. Conversely, M42h exhibits the smallest semicircle radius, indicating the fastest charge transfer kinetics [67]. The transfer resistance (R_{ct}) values of the four samples were derived via equivalent circuit modeling using ZView2 software (Fig. 5(e)). The conductivity relationship for the four samples is M42h > M0h > M50h > M58h, which aligns precisely with the observed ε'' trends. The frequency dependent dielectric loss tangent ($\tan\delta_\varepsilon$) curves (Fig. 5(c)) further elucidate the dielectric loss capabilities of MBT samples. M42h possesses superior dielectric loss capability due to its enhanced electrical conductivity, which effectively promotes conductive loss. Surprisingly, while M50h does not exhibit the highest conductivity among the four samples, it demonstrates substantial dielectric loss capabilities with significantly higher $\tan\delta_\varepsilon$ values in the frequency range of 7.6–18.0 GHz compared to M0h and M58h. This suggests that M50h demonstrates more significant capacity for polarization loss over conduction loss, which will be elaborated in the following section. Besides, the $\tan\delta_\varepsilon$ values are much larger than $\tan\delta_\mu$ values. The above results demonstrate that ball-milling induced defect engineering effectively modulates the complex permittivity, thereby optimizing the microwave absorption performance of MBT samples.

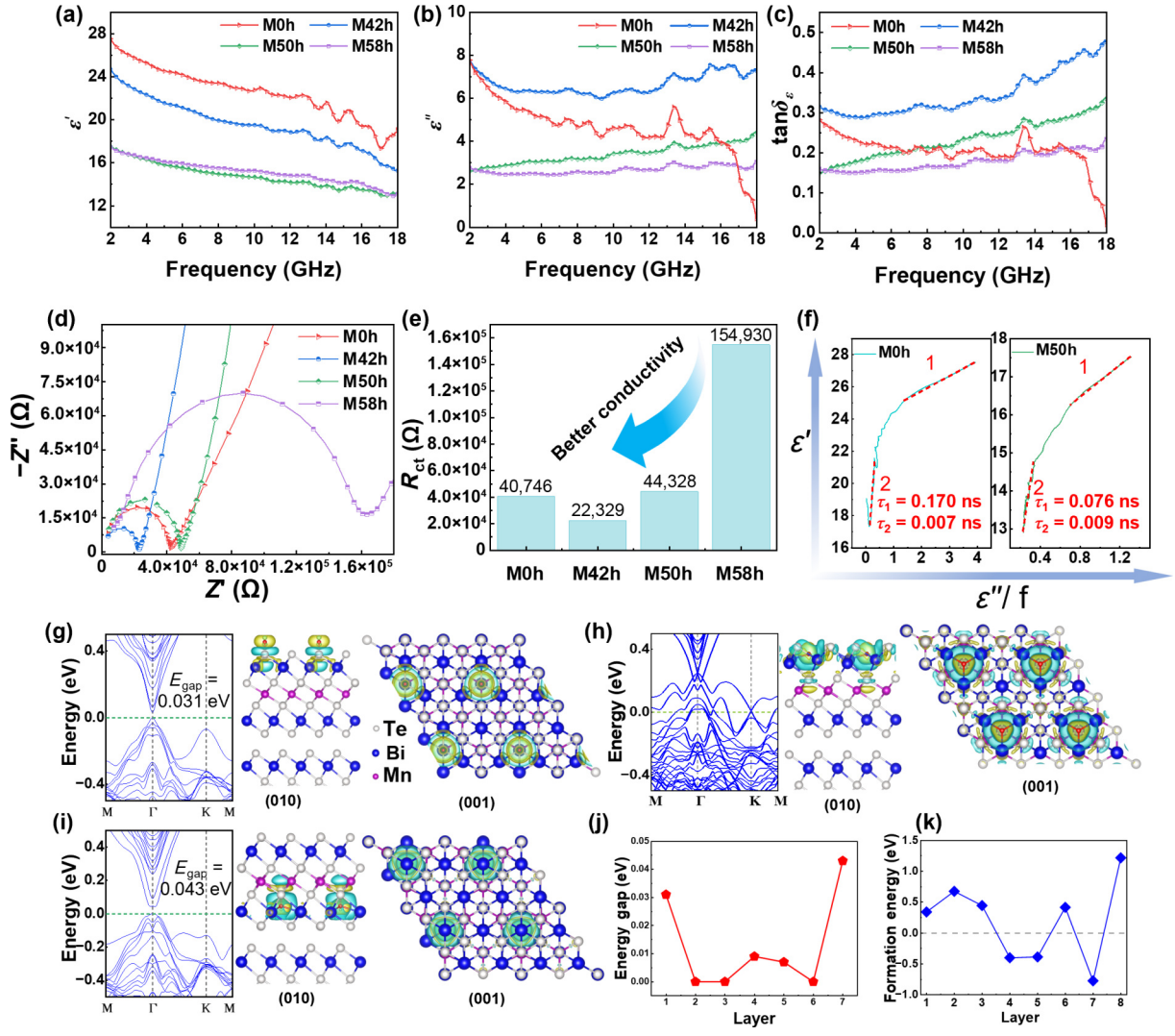

Figure 5 (a) Real part and (b) imaginary part of complex permittivity, (c) dielectric loss tangent (tanδ_ε), (d) Nyquist plots, and (e) electronic transfer resistance (R_{ct}) for M0h, M42h, M50h and M58h; (f) the relationship between ε' and ε''/f for M0h and M50h; the energy band and charge density distribution when oxygen atoms doped to (g) the first, (h) second, and (i) seventh atomic layer (yellow region indicates electron deposition, blue region indicates electron depletion); (j) the band gap and (k) corresponding formation energy of oxygen atoms doped in different atomic layers.

According to Debye relaxation theory, dielectric loss depends on the combined contribution of conduction loss and polarization loss. A semicircle formed in the ε'' versus ε' plot (Cole–Cole plot) represents a single Debye relaxation process, while a long straight tail in the plot indicates the presence of conduction losses [61]. To further analyze the dielectric loss mechanism, Cole–Cole plots were employed (Fig. S10 in the ESM), as derived from Eqs. (S6)–(S8) in the ESM. The linear segments observed at the curve termini confirm conductive loss in all samples. The presence of multiple irregular semicircular arcs in the Cole–Cole plot indicates multiple Debye relaxation processes within the MBT samples. Furthermore, the distorted semicircle morphology suggests additional dielectric loss mechanism beyond Debye relaxation processes, such as Maxwell–Wagner relaxation [8]. Combining the tanδ_ε values in Fig. 5(c) with the Cole–Cole plots in Fig. S10 in the ESM, it is reasonable to conclude that M50 exhibits moderate conduction loss alongside enhanced polarization relaxation loss compared to M0h, M42h and M58h samples. To further elucidate the polarization relaxation mechanisms in MBT samples, we determined the polarization relaxation time $\tau = 1/(2\pi k)$ by calculating the slope k of the linear relationship between ε' and ε''/f based on Eq. (S8) in the ESM. A linear functional relationship between ε' and ε''/f represents a single polarization relaxation process. Figure 5(f) and Fig. S11 in the ESM display plots of ε' versus ε''/f for all MBT samples. Two distinct slopes (k_1 and k_2) were fitted for each sample as marked by red dashed lines, indicating the coexistence of two types of polarization relaxation processes in all the MBT samples. Based on these fitted slopes, we calculated the corresponding polarization relaxation times τ_1 and τ_2:τ_1 (0.076–0.170 ns) in the low-frequency region and τ_2 (0.007–0.009 ns) in the high-frequency region. The longer relaxation time τ_1 corresponds to interfacial polarization. This is a macroscopic process involving slow charge migration across crystalline/amorphous interfaces in MBT samples, resulting in prolonged relaxation times. In contrast, the shorter relaxation time τ_2 originates from microcosmic dipolar and defect-induced polarization processes, that respond quickly to electric field. These details suggest that through the synergistic action of multiple relaxation processes and conduction loss, MBT samples achieves superior EMW absorption performance.

To systematically understand the dominant dielectric loss

mechanism and elucidate how ball milling-induced defect engineering enhances the intrinsic conductivity and multiple relaxation behavior, we conducted the subsequent specific analysis:

3.2.1 *The mechanism analysis of enhanced intrinsic conductivity*

Introduction of defects in MBT crystal effectively alters bulk/surface conductive states and topological properties [68–71]. A high density of defects in as-prepared MBT samples was proved by HRTEM images, XPS and electron paramagnetic resonance (EPR) spectrometer. Among them, oxygen-doping induced impurity defects generated during high-energy ball milling process is the most prevalent type of defect. Prolonged ball milling time leads to progressive oxidation, resulting in increased oxygen incorporation depth within the MBT lattice. Thus, we systematically investigated the correlation between electrical conductivity and the number of oxygen-doped layers (1–8 layers) by density functional theory (DFT) calculations. The formation energy in Fig. 5(k) suggests that Mn–O bonds (4th layer) and Te–O bonds (5th and 7th layer) are more stable than other metal–O bonds. Additionally, extending the oxygen doping to the top layer of next cell (8th layer) leads to a significant positive formation energy. This indicates that oxidation-induced defects are preferentially localized within the first two septuple-layer structures of MBT, which is consistent with previously reported experimental and theoretical results [72, 73].

Therefore, our discussion primarily focuses on the effects of oxygen doping from the 1st to the 7th layer in the unit cell. Figures 6(g)–6(i) and Fig. S12 in the ESM exhibit the energy band structures of optimized oxygen-doped models across 1–7 layers. Specifically, Fig. 5(j) compares the band gaps with oxygen doping at different layers. It is found that oxygen doping lead to a distinct layer-dependent electronic modulation effect: (1) oxygen doping in the 1st layer induces a characteristic direct band gap in MBT, suggesting semiconductor behavior; (2) oxygen doping in layers 2 to 6 leads to a sharp reduction in the band gap, indicating a significantly enhanced conductivity; (3) further oxygen doping up to the 7th layer results in a rapid reopening of the band gap, corresponding to a pronounced decreases in conductivity. This indicates that the electronic conductivity of MBT initially increases and subsequently decreases with progressive oxygen doping. These observations are consistent with the measured charge transfer resistance (R_{ct}) in Fig. 5(e). Besides, oxygen doping also exhibits bond-dependent electronic modulation effects: (1) The formation of Bi–O bonds results in a zero band gap, indicative of metallic behavior; (2) the formation of Mn–O bonds results in near zero (0.007 eV) band gap, suggesting a narrow-bandgap semiconductor with semi-metallic characteristic; (3) the formation of Te–O bonds leads to either metallic or semiconductor behavior, depending on the specific oxygen doping layer.

3.2.2 *Modulated polarization loss*

To elucidate the atomic-scale conductivity and polarization loss mechanisms, the charge densities distribution of optimized oxygen-doped models across layers 1–7 are displayed in Figs. 5(g)–5(i) and Fig. S12 in the ESM. The irregular yellow and blue parts in the charge density map represent the accumulation and dissipation of electrons, respectively. For shallow oxygen-doped layers (1–3 layers), electrons predominantly localize around oxygen atoms. This means that the oxygen doping enables the creation of additional polarization centers, thereby modulating electron concentration and facilitates the excitation of surrounding electrons under the influence of an external electric field. Furthermore, as defect states, oxygen doping can introduce additional defect energy levels, allowing electrons to encounter relatively low potential energy barriers in their vicinity [74]. Thus, the intrinsic conductivity of MBT initially increases after 42 h ball milling (Figs. 5(d) and 5(e)). It also explains that M42h obtains the highest ε'' (Fig. 5(b)). However, as oxygen doping extends to deeper layers (4–7 layers), the electron localization gradually decreases, evidenced by charge

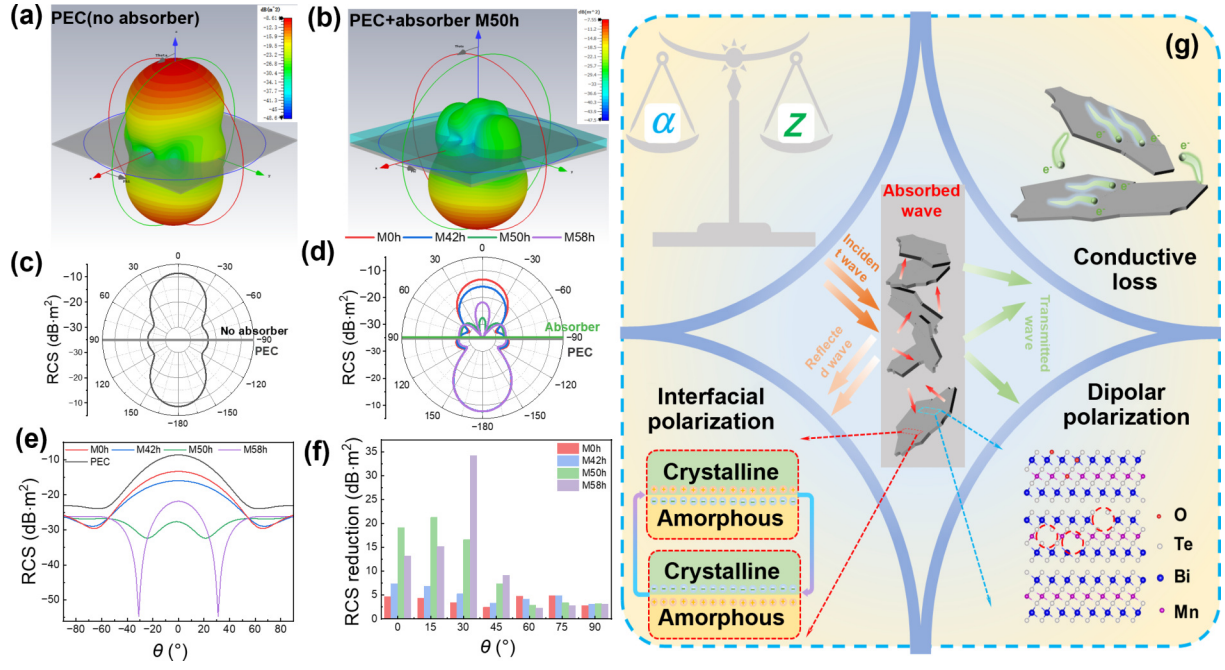

Figure 6 CST simulation results: 3D radar wave scattering plots of (a) PEC and (b) M50h + PEC. 2D RCS radiation diagrams of (c) PEC and (d) absorber (M0h, M42h, M50h, and M58h) + PEC. (e) Simulated RCS curves of M0h, M42h, M50h, and M58h within the scattering angle of −90°–90°; (f) RCS reduction values of M0h, M42h, M50h, and M58h. (g) EMW absorption mechanism diagram for MBT micro-flakes.

density (blue isosurfaces) progressively delocalizing into the surrounding lattice. This means the progressive weakening of oxygen-defect induced polarization with increasing doping depth. That is why the conductivity was reduced for M50h and M58h. In short, the oxygen-defect induced polarization and the formation of defect energy levels collectively explain how defect engineering modulates the intrinsic conductivity of MBT samples.

Based on the above discussion, the mechanism for the enhanced atomic-scale polarization loss is summarized as follows. First, the ball-milling process endows MBT samples with abundant oxygen doping defects and lattice defects. Under high-frequency electromagnetic fields, these defects trap charge carriers and disrupt the equilibrium of charge distribution, enables the creation of additional polarization centers, which effectively enhance the defect induced polarization relaxation. Second, multiple bonds are present in MBT samples, including Bi–Te, Mn/Bi–Te, Bi–O, and Te–O bonds, confirmed by XPS results. These chemical bonds serve as effective polarization centers that significantly enhance dipolar polarization relaxation process. Third, the crystalline/amorphous interfaces introduced during high-energy ball milling combined with the unique multilayer structure of MBT (as verified by SEM and HRTEM images) generate abundant heterointerfaces and significantly enhance interfacial polarization relaxation. Thus, it is concluded that the emergence of Debye relaxation processes in MBT samples (Fig. S10 in the ESM) arises from the synergistic effect of strong defect-induced polarization, dipole polarization, and interfacial polarization.

3.2.3 *Capacitor-like structure and conduction loss*

Due to the layered heterostructures of MBT samples (evidenced by SEM images in Fig. S1 in the ESM and Fig. 1), EMW interactions generate charge accumulation at heterointerfaces, forming space-charge regions. These space-charge regions function as capacitor-like structures (grain boundary capacitor layers), which effectively enhance charge storage capacity and lead to elevated real permittivity (ε') values [75]. However, high-energy ball milling treatment partially disrupts the layered heterostructures, resulting in a reduction of capacitor-like structures and consequently diminishing ε' values. This explains why prolonged ball milling duration leads to a decrease in ε' values of MBT samples (Fig. 5(a)). Besides, the interconnected MBT micro-flakes form an intricate conductive network. Upon exposure to external electromagnetic fields, mobile electrons flow along these conductive pathways, generating localized currents. The inherent resistance converts these currents into Joule heating, thereby dissipating EMW energy in the form of thermal energy.

Based on the above analysis, Fig. 6(g) schematically summarizes the enhanced EMW attenuation mechanism in MBT, with dielectric loss identified as the predominant factor. First, mutually stacked and interconnected MBT micro-flakes form an interconnected network, which facilitates the multi-scale scattering and refraction of EMW. This structure significantly extends the attenuation path and enhances conduction loss. Secondly, defect engineering optimizes polarization loss through controlled conductivity modulation and enhanced dipole/defect-induced polarization. Thirdly, the high-energy ball milling process introduces abundant crystalline/amorphous heterointerfaces, which promote interfacial charge accumulation and reinforce interfacial polarization. In summary, the synergistic combination of conduction loss and polarization loss endows MBT samples with superior impedance matching. Benefiting from the excellent impedance matching, the incident EMW energy efficiently converted into thermal energy and dissipated, thereby resulting in robust EMW absorption.

3.3 EW dissipation capacity evaluated by theoretical simulations

To assess the practical applications of MBT samples in EMW absorption, the far-field EM dissipation capacity of MBT-based materials was quantitatively evaluated by radar cross section (RCS) simulations using CST software. As shown in Fig. S13(a) in the ESM, the absorber was modeled as a coating on a perfect electric conductor (PEC) substrate [76]. Figures 6(a) and 6(b), and Figs. S13(b) and S13(d) in the ESM display the 3D radar scattering patterns of PEC and MBT samples coated PEC (absorber + PEC). PEC exhibits maximum radar scattering intensity (Fig. 6(a)). In contrast, RCS values of M50h + PEC significantly reduce compared to bare PEC across the angular range of $-90° < \theta < 90°$ (Fig. 6(b)), demonstrating that MBT samples can effectively suppress radar scattering intensity. 2D radar scattering patterns and the comparison of RCS values for all samples are displayed in Figs. 6(c)–6(e). M0h, M42h, and M58h samples exhibit partial radar scattering suppression, which is significantly weaker than that of M50h sample. To precisely evaluate the inherent energy dissipation capability of different coatings, the RCS reduction across −90° to 90° was calculated by subtracting the RCS value of PEC substrate [77], as illustrated in Fig. 6(f) and Fig. S13(e) in the ESM. M50h sample displays superior radar wave attenuation (below −25 dB) over a broad angular range (−90°–90°). M58h sample demonstrates the strongest radar wave attenuation at 30°, reaching a maximum reduction of 40.5 dB·m^2. These results demonstrate that defect engineering successfully optimizes both impedance matching and attenuation capability, enabling efficient EMW energy dissipation and radar scattering intensity suppression.

4 Conclusion

In summary, we developed a green strategy for effective and progressive defect engineering in MBT micro-flakes (dominated by oxidation doping), which significantly improves the microwave absorption performance, especially for high-frequency absorption. By systematically adjusting high-energy ball milling duration (0, 42, 50, 58 h), gradient oxidation doping was achieved, which promotes the excitation of surrounding electrons and formation of additional polarization centers. Furthermore, the multilayer architecture at macroscopic scale and crystalline/amorphous heterointerfaces at microcosmic scale, introduced during high-energy ball milling, not only create abundant capacitor-like structures that enhance the storage of microwave energy but also promote multiple reflections of EMW. Combined with the modulated intrinsic electric conductivity and enhanced polarization loss, these effects significantly optimize impedance matching characteristics and broaden the effective absorption bandwidth. Consequently, 50 h ball-milled MBT exhibits superior overall microwave absorption performance, achieving a RL_{min} of −61.99 dB at 3.30 GHz. The EAB_{max} increased from 2.26 GHz (4.97–3.10 GHz & 16.90–18 GHz) to 3.63 GHz (14.37–18 GHz) compared to the pristine MBT, representing a 61% enhancement. Furthermore, the M50h sample demonstrates excellent radar wave attenuation ability, with a reduced RCS value of −25 dB across an extremely broad angle range (−90°–90°). These results demonstrate that high-energy ball milling is an effective strategy for constructing defect engineering in

MBT to notably optimizes dielectric properties and improves impedance matching characteristics, therefore significantly enhancing the intrinsic microwave absorption performance. Furthermore, these findings provide novel and valuable insights that expand the research and application of topological materials as advanced microwave-absorption candidates.

Electronic Supplementary Material: Supplementary material is available in the online version of this article at https://doi.org/10.26599/NR.2026.94908362.

Data availability

All data needed to support the conclusions in the paper are presented in the manuscript and the Electronic Supplementary Material. Additional data related to this paper may be requested from the corresponding author upon request.

Acknowledgements

This work was supported by the National Natural Science Foundation of China (Nos. 92365204, 51991343, 21975140, and 51872021) and Fundamental Research Funds for the Central Universities (No. buctrc202212).

Declaration of competing interest

The authors declare that they have no known competing financial interests or personal relationships that could have appeared to influence the work reported in this paper.

Author contribution statement

G. L. H.: Writing – original draft, investigation, data curation, project administration, validation, experimental design. D. W. L.: Investigation. P. P. Z.: Software. Y. B. S.: Resources. J. H. H.: Validation, investigation. Z. S. J.: Investigation. Y. L. S.: Investigation. J. M. W.: Validation. Y. W.: Writing – review & editing, validation, conceptualization. N. N. S.: Writing – review & editing, supervision, project administration, methodology. All the authors have approved the final manuscript.

Use of AI statement

None.

References

[1] Zhang, J.; Chen, J.; Liu, Z. K.; Ma, Y. Z.; Wang, X. L.; Yang, X. F.; Que, M. D.; Li, Y. J. *In situ* growing CNTs/TiO_2 heterojunction on MXene sheets for enhanced microwave absorption via multiple electron transfer paths and polarization. *Ceram. Int.* **2024**, *50*, 2282–2292.

[2] Wang, B. L.; Ni, C.; Xie, X. B.; Ding, M. C.; Li, C. W. Carbon nanotubes-encapsulated Co/Co_7Fe_3 nanocomposites: Achieving wideband electromagnetic wave absorption at ultrathin-thickness by regulating magnetic phase ratio. *Chem. Eng. J.* **2024**, *494*, 153076.

[3] Liu, C.; Wu, N.; Pan, F.; Zhang, X.; Wang, Z.; Wu, L. L.; Lin, J. P.; Liu, W.; Liu, J. R.; Zeng, Z. H. Graphene/carbon nanotube aerogels with ultralow filling ratio through perfect cross-linking interface for efficient microwave absorption. *Compos. B: Eng.* **2024**, *287*, 111835.

[4] Li, L. H.; Liu, G. M.; Wei, S. C.; Zhang, Q.; Shi, R. D.; Wang, Y. J.; Wang, B.; Liu, Z.; Huang, K. N.; Wang, X. Y. et al. Facile synthesis of nickel ferrite decorated carbon nanotube/cellulose aerogel for efficient electromagnetic wave absorption. *Small Methods* **2025**, *9*, 2402260.

[5] Shi, X. F.; You, W. B.; Li, X.; Wang, L.; Shao, Z. Z.; Che, R. C. *In-situ* regrowth constructed magnetic coupling 1D/2D Fe assembly as broadband and high-efficient microwave absorber. *Chem. Eng. J.* **2021**, *415*, 128951.

[6] Qiu, J. F.; Liu, X.; Peng, C. Y.; Wang, S. H.; Wang, R. C.; Wang, W. Porous metal microsphere M@C-rGO (metal = Mn, Fe, Co, Ni, Cu) aerogels with high low-frequency microwave absorption, strong thermal insulation and superior anticorrosion performance. *J. Mater. Chem. A* **2024**, *12*, 21997–22012.

[7] Su, L.; Han, R.; Wang, J. M.; He, J. H.; Huang, G. L.; Wang, X. Y.; Gong, Z. Z.; Yang, X.; Song, N. N. Enhanced microwave absorption performance of $Sm_2Fe_{14}B$ microflakes with adjustable bianisotropy. *J. Alloys Compd.* **2025**, *1037*, 182216.

[8] Du, J. W.; Zhang, M. Y.; Tang, P.; Zhang, L. W.; Zhao, X. Y.; Zhan, X. L.; Wang, B.; Zhao, J. J.; Liu, N. N.; Wu, G. H. et al. Enhanced low-frequency electromagnetic wave absorption by CoFe alloy/C microspheres synthesized from metal-organic frameworks. *J. Alloys Compd.* **2025**, *1010*, 177936.

[9] Sutar, R. B.; Kulkarni, G. K.; Koli, R. R.; Dhas, S. D.; Velhal, N. B.; Rajpure, K. Y.; Puri, V. R.; Yadav, J. B. Bio-derived graphitic carbon microspheres: A green approach for high-frequency microwave absorption. *Diam. Relat. Mater.* **2025**, *151*, 111836.

[10] Kong, L.; Qi, J.; Li, M. H.; Chen, X. Y.; Yuan, X. Y.; Wang, T.; Yang, J.; Huang, J. F.; Fan, X. M. Electromagnetic wave absorption properties of $Ti_3C_2T_x$ nanosheets modified with *in-situ* growth carbon nanotubes. *Carbon* **2021**, *183*, 322–331.

[11] Gang, S.; He, H.; Long, H.; Wei, Y. C.; Zhang, W. G.; Li, X.; Qian, Y. X.; Luo, Y. B.; Yang, J. Y. 2D-high entropy alloys embedded in 3D-carbon foam towards light-weight electromagnetic wave absorption and hydrophobic thermal insulation. *Nano Energy* **2025**, *135*, 110642.

[12] Wang, Y. S.; Fang, L. Y.; Xu, C. R.; Chen, X. L.; Lu, Z. Y.; Xu, G. L.; Yang, L. W.; Ouyang, Y. F.; Tao, X. M. Excellent electromagnetic wave absorption performances of FeCoNiAlTi$_x$ high-entropy alloys with superior oxidation resistance. *J. Mater. Chem. C* **2025**, *13*, 4583–4593.

[13] Zhang, L.; Huo, Y. S.; Liu, Y.; Zhao, M. S.; Tan, Y. J.; Huo, S. Y.; Yao, L.; Qu, S. H.; He, Z. H. Design and synthesis of non-homogeneous CoS_2/carbon composite nanofibers for enhanced microwave absorption. *Carbon* **2025**, *236*, 120120.

[14] Liu, J. L.; Wang, M.; Zhang, L. M.; Zang, D. Y.; Liu, H.; Francesca Liotta, L.; Wu, H. J. Tunable sulfur vacancies and hetero-interfaces of FeS_2-based composites for high-efficiency electromagnetic wave absorption. *J. Colloid Interface Sci.* **2021**, *591*, 148–160.

[15] Jiang, J. J.; Deng, X. M.; Li, S. H.; Zeng, X. J.; Wu, C. X.; Yang, C. Hierarchically porous multiphase Si-based ceramics with synergistic electromagnetic wave absorption mechanisms (Adv. Sci. 42/2025). *Adv. Sci.* **2025**, *12*, 72373.

[16] Xiong, L. Y.; Chen, H. J.; Mo, G. M.; Huang, Q. Synthesis of fine-grained polycarbosilane-derived Ti_3SiC_2 with high-phase-fraction and investigation of their microwave absorption properties. *Small* **2025**, *21*, e04884.

[17] Chen, J. B.; Liang, X. H.; Quan, B.; Yang, Z. H.; Du, Y. W.; Ji, G. B. 3D flake-like Bi_2Te_3 with outstanding lightweight electromagnetic wave absorption feature. *Part. Part. Syst. Charact.* **2018**, *35*, 1700468.

[18] Fu, L. Topological crystalline insulators. *Phys. Rev. Lett.* **2011**, *106*, 106802.

[19] Park, K.; Heremans, J. J.; Scarola, V. W.; Minic, D. Robustness of topologically protected surface states in layering of Bi_2Te_3Thin films. *Phys. Rev. Lett.* **2010**, *105*, 186801.

[20] Tang, M.; Zhang, J. Y.; Bi, S.; Hou, Z. L.; Shao, X. H.; Zhan, K. T.;

Cao, M. S. Ultrathin topological insulator absorber: Unique dielectric behavior of Bi_2Te_3 nanosheets based on conducting surface states. *ACS Appl. Mater. Interfaces* **2019**, *11*, 33285–33291.

[21] Long, H.; Qian, Y. X.; Gang, S.; Zhang, W. G.; Yang, B. Y.; Wei, Y. C.; Wang, B.; Li, W.; Jiang, Q. H. High-performance thermoelectric composite of Bi_2Te_3 nanosheets and carbon aerogel for harvesting of environmental electromagnetic energy. *ACS Nano* **2025**, *19*, 1819–1831.

[22] Liu, X. H.; Cai, J. N.; Zhang, J. Y.; Zhao, P. Y.; Wang, G. S.; Bi, S.; Hou, Z. L. Surface-state-constrained topological insulator Bi_2Te_3 nanorods for electromagnetic wave trapping and conversion into electricity. *J. Mater. Sci. Technol.* **2026**, *244*, 149–155.

[23] Lee, D. S.; Kim, T. H.; Park, C. H.; Chung, C. Y.; Lim, Y. S.; Seo, W. S.; Park, H. H. Crystal structure, properties and nanostructuring of a new layered chalcogenide semiconductor, Bi_2MnTe_4. *CrystEngComm* **2013**, *15*, 5532–5538.

[24] Li, G. M.; Wu, X. H.; Gao, Y. F.; Ma, X. M.; Hou, F. C.; Cheng, H. Y.; Huang, Q. L.; Wu, Y. C.; DeCapua, M. C.; Zhang, Y. J. et al. Observation of ultrastrong coupling between substrate and the magnetic topological insulator $MnBi_2Te_4$. *Nano Lett.* **2022**, *22*, 3856–3864.

[25] Guo, H.; Bai, C. Y.; Zhu, K.; Lv, S. H.; Zhai, Z. Y.; Qu, J. Y.; Xian, G. Y.; Han, Y. C.; Hu, G. J.; Qi, Q. et al. Controllable synthesis of high-quality magnetic topological insulator $MnBi_2Te_4$ and $MnBi_4Te_7$ multilayers by chemical vapor deposition. *Nano Lett.* **2024**, *24*, 15788–15795.

[26] Hou, F. C.; Yao, Q. S.; Zhou, C. S.; Ma, X. M.; Han, M. J.; Hao, Y. J.; Wu, X. F.; Zhang, Y.; Sun, H. Y.; Liu, C. et al. Te-vacancy-induced surface collapse and reconstruction in antiferromagnetic topological insulator $MnBi_2Te_4$. *ACS Nano* **2020**, *14*, 11262–11272.

[27] Bartram, F. M.; Leng, Y. C.; Wang, Y. C.; Liu, L. Y.; Chen, X.; Peng, H. N.; Li, H.; Yu, P.; Wu, Y.; Lin, M. L. et al. Ultrafast coherent interlayer phonon dynamics in atomically thin layers of $MnBi_2Te_4$. *npj Quantum Mater.* **2022**, *7*, 84.

[28] Deng, Y. J.; Yu, Y. J.; Shi, M. Z.; Guo, Z. X.; Xu, Z. H.; Wang, J.; Chen, X. H.; Zhang, Y. B. Quantum anomalous Hall effect in intrinsic magnetic topological insulator $MnBi_2Te_4$. *Science* **2020**, *367*, 895–900.

[29] Ovchinnikov, D.; Huang, X.; Lin, Z.; Fei, Z. Y.; Cai, J. Q.; Song, T. C.; He, M. H.; Jiang, Q. N.; Wang, C.; Li, H. et al. Intertwined topological and magnetic orders in atomically thin chern insulator $MnBi_2Te_4$. *Nano Lett.* **2021**, *21*, 2544–2550.

[30] Fan, Z. D.; Xu, H. H.; Zhao, J. G.; Zhang, Y. H.; Wang, X. J.; Sui, Y.; Lv, Z.; Liu, J.; Jiang, S. D.; Liu, Z. G. Crystal growth and magnetic evolution of antiferromagnetic topological insulator Zn-doped $MnBi_2Te_4$. *J. Solid State Chem.* **2025**, *345*, 125242.

[31] Chen, Z. G.; Li, J.; Xu, T. T.; Zhang, Z. Y.; Zhao, D. P.; Zhou, Z. X. Ingenious microstructure combination through topological surface state enabled $MnBi_2Te_4$/carbon fibers to be an ultrathin absorber. *Appl. Phys. Lett.* **2024**, *124*, 071902.

[32] Gao, Z. G.; Ma, Z. H.; Lan, D.; Zhao, Z. H.; Zhang, L. M.; Wu, H. J.; Hou, Y. L. Synergistic polarization loss of MoS_2-based multiphase solid solution for electromagnetic wave absorption. *Adv. Funct. Mater.* **2022**, *32*, 2112294.

[33] Chen, G.; Liang, H. S.; Yun, J. J.; Zhang, L. M.; Wu, H. J.; Wang, J. Y. Ultrasonic field induces better crystallinity and abundant defects at grain boundaries to develop cus electromagnetic wave absorber. *Adv. Mater.* **2023**, *35*, 2305586.

[34] Gong, C. C.; Ding, J. W.; Wang, C. X.; Zhang, Y. J.; Cong, H. W.; Liu, H. J.; Guo, Y.; Song, K.; Shi, C. S.; He, F. Utilizing Se vacancies as electronic traps to synergize impedance matching and dipole polarization with ultrathin strategy to boost Fe–Se electromagnetic wave absorption. *Chem. Eng. J.* **2024**, *480*, 147793.

[35] Xie, L.; Liu, R. L.; Jiang, X. M.; Ni, C.; Wang, B. L.; Hou, C. X.; Lan, D.; Du, W.; Xie, X. B. Carbon induced multiple interfaces and *in-situ* formed defects in oxidation of Co toward enhancing microwave absorption performances. *Carbon* **2025**, *238*, 120272.

[36] Feng, X. R.; Hou, X.; Zheng, Y. C.; Jiang, K.; Liu, J. T.; Wang, M. Defect engineering on carbon nanotubes or graphene to balance conduction and polarization loss for enhancing microwave absorption. *ACS Appl. Nano Mater.* **2025**, *8*, 813–827.

[37] Qin, L. Y.; Guo, Z. Y.; Shu, Q. H.; Lv, L.; Jia, L.; Yang, Y.; Jiang, W.; Lv, X. J.; Zhou, J. D. Activating basal plane inert sites of iron telluride for motivational electromagnetic microwave absorption (Small 36/2025). *Small* **2025**, *21*, e70315.

[38] Zuo, X. Q.; Zhang, Y. F.; Tian, J.; Sun, C.; Wen, N. X.; Zhang, H.; Li, C. W.; Fan, Z.; Pan, L. J. Fabrication of micro-mesopores on spiral carbon nanocoils and simultaneous doping with oxygen to expand microwave absorption bandwidth. *Adv. Funct. Mater.* **2024**, *34*, 2410224.

[39] Dai, J. A.; Zhang, S. J.; Wang, F.; Wen, L.; Sun, Y. H.; Ren, K.; Xu, Y. H.; Zeng, W.; Wang, S. L. A new *in situ* oxidized 2D layered $MnBi_2Te_4$ cathode for high-performance aqueous zinc-ion battery. *Small* **2024**, *20*, 2307033.

[40] Cai, Y. H.; Begin, D.; Lefevre, C.; Sidhoum, C.; Elkaim, E.; Boulet, P.; Desgardin, P.; Barthe, M. F.; Helm, R.; Egger, W. et al. Enhanced electromagnetic wave absorption in $Mapbi_3$ hybrid perovskite through a defect-tunable green synthesis. *Small Struct.* **2025**, *6*, 2500066.

[41] Li, H.; Liu, S. S.; Liu, C.; Zhang, J. S.; Xu, Y.; Yu, R.; Wu, Y.; Zhang, Y. G.; Fan, S. S. Antiferromagnetic topological insulator $MnBi_2Te_4$: Synthesis and magnetic properties. *Phys. Chem. Chem. Phys.* **2020**, *22*, 556–563.

[42] Tang, J.; Wu, Y. D.; Wang, W. W.; Kong, L. Y.; Lv, B. Y.; Wei, W. S.; Zang, J. D.; Tian, M. L.; Du, H. F. Magnetic skyrmion bundles and their current-driven dynamics. *Nat. Nanotechnol.* **2021**, *16*, 1086–1091.

[43] Hossain, M.; Qin, B.; Li, B.; Duan, X. D. Synthesis, characterization, properties and applications of two-dimensional magnetic materials. *Nano Today* **2022**, *42*, 101338.

[44] Li, Q. F.; Zhang, X.; Chen, Z. H.; Li, W.; Ma, H. R.; Chen, Y.; Guan, J. G. Improving interfacial magnetoelastic effect and complex permeability of FeSiAl alloy powders for broadband decimeter-wave absorption via Cr doping. *J. Alloys Compd.* **2024**, *1002*, 175248.

[45] Chen, N. K.; Wang, C.; Xiao, Y. Y.; Han, R.; Wu, Q.; Song, N. N. Tunable microwave absorption properties of anisotropic Nd_2Co_{17} micro-flakes. *J. Alloys Compd.* **2023**, *947*, 169554.

[46] Xiong, X. H.; Zhang, H. B.; Lv, H. L.; Yang, L. T.; Liang, G. S.; Zhang, J. C.; Lai, Y. X.; Cheng, H. W.; Che, R. C. Recent progress in carbon-based materials and loss mechanisms for electromagnetic wave absorption. *Carbon* **2024**, *219*, 118834.

[47] Wu, P. K.; Kong, X. K.; Feng, Y. R.; Ding, W.; Sheng, Z. G.; Liu, Q. C.; Ji, G. B. Phase engineering on amorphous/crystalline γ-Fe_2O_3 nanosheets for boosting dielectric loss and high-performance microwave absorption. *Adv. Funct. Mater.* **2024**, *34*, 2311983.

[48] Qin, M.; Zhang, L. M.; Wu, H. J. Dielectric loss mechanism in electromagnetic wave absorbing materials. *Adv. Sci.* **2022**, *9*, 2105553.

[49] Zeugner, A.; Nietschke, F.; Wolter, A. U. B.; Gaß, S.; Vidal, R. C.; Peixoto, T. R. F.; Pohl, D.; Damm, C.; Lubk, A.; Hentrich, R. et al. Chemical aspects of the candidate antiferromagnetic topological insulator $MnBi_2Te_4$. *Chem. Mater.* **2019**, *31*, 2795–2806.

[50] Jamwal, U.; Singh, D.; Yadav, K. L. Development of CI/BFO nanocomposite for efficient microwave absorption in low frequency range of L, S, C, and X-bands. *J. Alloys Compd.* **2023**, *968*, 171798.

[51] Cho, Y.; Kang, J. H.; Liang, L. B.; Taylor, M.; Kong, X. R.; Ghosh, S.; Kargar, F.; Hu, C. W.; Balandin, A. A.; Puretzky, A. A. et al. Phonon modes and Raman signatures of $MnBi_{2n}Te_{3n+1}$ (n = 1, 2, 3, 4) magnetic topological heterostructures. *Phys. Rev. Res.* **2022**, *4*, 013108.

[52] Wen, L.; Zhang, Q. X.; Shi, J. J.; Wang, F.; Wang, S. L.; Chen, Z. W.; Yue, Y.; Gao, Y. H. Layered topological insulator $MnBi_2Te_4$ as a cathode for a high rate performance aqueous zinc-ion battery. *ACS Nano* **2024**, *18*, 5981–5990.

[53] Deng, H. Q.; Zhang, Y.; Yang, X. X.; Yu, Q.; Wang, P. D.; Yang, Z. X.; Dai, Y. P.; Pang, X. Y.; Wang, X.; Wu, J. et al. Magnetic topological insulator $MnBi_2Te_4$ nanosheets for femtosecond pulse generation. *ACS Appl. Mater. Interfaces* **2023**, *15*, 47250–47259.

[54] Chen, X.; Zhang, X.; Li, Y. H.; Qi, M. Y.; Li, J. Y.; Tang, Z. R.; Zhou, Z.; Xu, Y. J. Transition metal doping BiOBr nanosheets with oxygen vacancy and exposed {102} facets for visible light nitrogen fixation. *Appl. Catal. B: Environ.* **2021**, *281*, 119516.

[55] Yi, H. L.; Wang, Y. H.; Diao, L. L.; Xin, Y. J.; Chai, C.; Cui, D. J.; Ma, D. Ultrasonic treatment enhances the formation of oxygen vacancies and trivalent manganese on α-MnO_2 surfaces: Mechanism and application. *J. Colloid Interface Sci.* **2022**, *626*, 629–638.

[56] Yu, J.; Zhang, C.C.; Zhou, L.; Koo, M. C.; Sun, X. B.; Wang, G. S. Enhanced microwave-absorbing performances for phthalocyanine/MXene nanocomposites by constructing oxygen vacancies. *Nano Res.* **2025**, *18*, 94907624.

[57] Hu, X. Y.; Wang, J. T.; Wang, J.; Deng, Y.; Zhang, H. D.; Xu, T.; Wang, W. L . β particles induced directional inward migration of oxygen vacancies: Surface oxygen vacancies and interface oxygen vacancies synergistically activate PMS. *Appl. Catal. B: Environ.* **2022**, *318*, 121879.

[58] Miao, Y. K.; Cui, A. G.; Wang, C.; Tian, Z. N.; Wang, T.; Liu, J. Y.; Jia, Q. Q.; Li, Z. J.; Zhang, M. Regulating oxygen vacancies to enhance dipole and interface polarization for highly efficient electromagnetic wave absorption in SiC@MnO_2 nanocomposites. *Adv. Funct. Mater.* **2025**, *35*, 2503394.

[59] Huang, G. L.; Zhu, S. X.; He, J. H.; Wu, Q.; Jing, Z. S.; Shen, Y. L.; Song, N. N. N-doped carbon nanotubes encapsulated NdCo micro-flakes for excellent microwave absorption and effective anti-corrosion performance. *Appl. Surf. Sci.* **2025**, *713*, 164308.

[60] Xu, Z. G.; Du, J. H.; Wang, J.; Chen, Z. H.; Li, W. J.; Wang, C. B.; Shen, Q. A comparative study on the microwave absorption properties of core-single-shell, core-double-shell and yolk-shell CIP/ceramic composite microparticles. *J. Magn. Magn. Mater.* **2022**, *547*, 168959.

[61] Cheng, H. R.; Pan, Y. M.; Li, W.; Liu, C. T.; Shen, C. Y.; Liu, X. H.; Pan, C. F. Facile design of multifunctional melamine foam with Ni-anchored reduced graphene oxide/MXene as highly efficient microwave absorber. *Nano Today* **2023**, *52*, 101958.

[62] Zhong, S. C.; Wang, J. Y.; Zhang, X. T.; Liu, Y.; Wang, X. Y.; Han, X. Z.; Zhang, P. P.; Xia, L. Trilayer core-shell FeCo@SiO_2@lithium-aluminum-silicate microspheres for electromagnetic wave absorption. *ACS Appl. Nano Mater.* **2024**, *7*, 15663–15674.

[63] Wang, M. Q.; Lin, Y.; Yang, H. B.; Qiu, Y.; Wang, S. A novel plate-like $BaFe_{12}O_{19}$@MoS_2 core–shell structure composite with excellent microwave absorbing properties. *J. Alloys Compd.* **2020**, *817*, 153265.

[64] Liu, J. L.; Zhang, L. M.; Zang, D. Y.; Wu, H. J. A competitive reaction strategy toward binary metal sulfides for tailoring electromagnetic wave absorption. *Adv. Funct. Mater.* **2021**, *31*, 2105018.

[65] Liu, Y. J.; Zhou, J. T.; Li, C. C.; Zhang, H. H.; Wang, Y. C.; Yan, Y.; Duan, L.; Cheng, Z. Y.; Ma, Y.; Yao, Z. J. Interfacial coupling effects in two-dimensional ordered arrays for microwave attenuation. *Nat. Commun.* **2025**, *16*, 202.

[66] Liang, Q. Q.; He, M. K.; Zhan, B. B.; Guo, H.; Qi, X. S.; Qu, Y. P.; Zhang, Y. L.; Zhong, W.; Gu, J. W. Yolk-shell CoNi@N-doped carbon-CoNi@CNTs for enhanced microwave absorption, photothermal, anti-corrosion, and antimicrobial properties. *Nano-Micro Lett.* **2025**, *17*, 167.

[67] Huang, W. H.; Song, M.; Wang, S.; Wang, B. K.; Ma, J. C.; Liu, T.; Zhang, Y. N.; Kang, Y. F.; Che, R. C. Dual-step redox engineering of 2D CoNi-Alloy embedded B, N-doped carbon layers toward tunable electromagnetic wave absorption and light-weight infrared stealth heat insulation devices. *Adv. Mater.* **2024**, *36*, 2403322.

[68] Konopko, L.; Nikolaeva, A.; Huber, T. E.; Rogacki, K. Quantum oscillations in nanowires of topological insulator $Bi_{0.83}Sb_{0.17}$. *Appl. Surf. Sci.* **2020**, *526*, 146750.

[69] Xie, B. Y.; Liu, H.; Wang, H. N.; Cheng, H.; Tian, J. G.; Liu, Z. Y.; Chen, S. Q. Tailoring the surface and interface states in a three-dimensional fragile topological insulator with kagome lattice. *Phys. Rev. B* **2022**, *106*, 115305.

[70] Du, M. H.; Yan, J. Q.; Cooper, V. R.; Eisenbach, M. Tuning fermi levels in intrinsic antiferromagnetic topological insulators $MnBi_2Te_4$ and $MnBi_4Te_7$ by defect engineering and chemical doping. *Adv. Funct. Mater.* **2021**, *31*, 2006516.

[71] Su, S. H.; Chang, J. T.; Chuang, P. Y.; Tsai, M. C.; Peng, Y. W.; Lee, M. K.; Cheng, C. M.; Huang, J. C. A. Epitaxial growth and structural characterizations of $MnBi_2Te_4$ thin films in nanoscale. *Nanomaterials* **2021**, *11*, 3322.

[72] Akhgar, G.; Li, Q. L.; Di Bernardo, I.; Trang, C. X.; Liu, C.; Zavabeti, A.; Karel, J.; Tadich, A.; Fuhrer, M. S.; Edmonds, M. T. Formation of a stable surface oxide in $MnBi_2Te_4$ thin films. *ACS Appl. Mater. Interfaces* **2022**, *14*, 6102–6108.

[73] Mazza, A. R.; Lapano, J.; MeyerIii, H. M.; Nelson, C. T.; Smith, T.; Pai, Y. Y.; Noordhoek, K.; Lawrie, B. J.; Charlton, T. R.; Moore, R. G. et al. Surface-driven evolution of the anomalous hall effect in magnetic topological insulator $MnBi_2Te_4$ thin films. *Adv. Funct. Mater.* **2022**, *32*, 2202234.

[74] Hui, S. C.; Chen, Q.; Tao, K.; Zhang, L. M.; Fan, X. M.; Che, R. C.; Wu, H. J. Highly mixed index facet engineering induces defect formation and converts the wave-transmissive mott insulator NiO into electromagnetic wave absorbent. *Adv. Mater.* **2025**, *37*, 2415844.

[75] Shao, C. S.; Ding, C. Y.; Liu, Y.; Ma, Y.; Zhang, L.; Ren, X. Z.; Wu, S. S.; Zhong, B.; Wen, G. W.; Huang, X. X. Grain boundary capacitance effect in Iron-based magnetic composites for superior C-band microwave absorption. *Chem. Eng. J.* **2023**, *466*, 143162.

[76] Ma, Z. H.; Yang, K.; Li, D.; Liu, H.; Hui, S. C.; Jiang, Y. Y.; Li, S. Y.; Li, Y. M.; Yang, W.; Wu, H. J. et al. The electron migration polarization boosting electromagnetic wave absorption based on Ce atoms modulated yolk@shell Fe_xN@NGC. *Adv. Mater.* **2024**, *36*, 2314233.

[77] Wang, C.; Chen, N. K.; Xiao, Y. Y.; He, J. H.; Han, R.; Song, N. N. Exceeding natural resonance frequency limit and enhanced microwave absorption performance of Fe_3O_4 nanorods coated with SiO_2 layer. *Ceram. Int.* **2023**, *49*, 36233–36243.